Published in final edited form as:
Nat Neurosci. 2018 July ; 21(7): 974–984. doi:10.1038/s41593-018-0164-7.

Thalamic dual control of sleep and wakefulness

Thomas C. Gent[1], **Mojtaba Bandarabadi**[1], **Carolina Gutierrez Herrera**[1], and **Antoine R. Adamantidis**[1,2,*]

[1]Centre for Experimental Neurology, Department of Neurology, Inselspital University Hospital, University of Bern, Bern, Switzerland [2]Department of Clinical Research, Inselspital University Hospital, University of Bern, Bern, Switzerland

Abstract

Slow-waves (0.5 - 4 Hz) predominate in the cortical electroencephalogram during non-rapid eye movement (NREM) sleep in mammals. They reflect the synchronization of large neuronal ensembles alternating between active (UP) and quiescent (Down) states and propagating along the neocortex. The thalamic contribution to cortical UP-states and sleep modulation remains unclear. Here we show that spontaneous firing of centromedial thalamus (CMT) neurons in mice is phase advanced to global cortical UP-states and NREM–wake transitions. Tonic optogenetic activation of CMT neurons induces NREM–wake transitions, whereas burst activation mimics UP-states in the cingulate cortex (CING) and enhances brain-wide synchrony of cortical slow-waves during sleep, through a relay in the antero-dorsal thalamus (AD). Finally, we demonstrate that CMT and AD relay neurons promote sleep recovery. These findings suggest that the firing pattern of CMT neurons can modulate brain-wide cortical activity during sleep and provides dual control of sleep-wake states.

Introduction

Non-rapid eye movement sleep (NREM) is characterized by a predominance of slow-waves (0.5 - 4 Hz) in the neocortex resulting from the synchronized activity of thalamo-cortical

*Correspondence should be addressed to: Antoine Adamantidis, Ph.D., Dept of Neurology, Inselspital University Hospital, University of Bern, Freiburgstrasse, 18, 3010 Bern, Switzerland, Tel: +41 (0)31 632 55 93, antoine.adamantidis@dbmr.unibe.ch.

Reporting Summary
Further information on experimental design is available in the Life Sciences Reporting Summary linked to this article.

Data and Code Availability
The data that support the findings of this study and the Matlab code used for analysis are available from the corresponding author upon reasonable request.

Author Contributions
T.G. and A.A. conceived the study. T.G. and C.G.H. collected the data. T.G. and M.B. analyzed the data. A.A. supervised the project. All authors wrote the manuscript.

The authors declare no competing financial interests.

Author Information
Reprints and permissions information are available at www.nature.com/reprints. Readers are welcome to comment on the online version of the paper.

Europe PMC Funders Author Manuscripts

neuronal networks alternating between active (UP) and quiescent (DOWN) states1–3. During UP-states, the membrane potentials of neocortical pyramidal neurons and interneurons are depolarized, which facilitates spiking activity, whereas DOWN-states reflect cell membrane hyperpolarization and neuron spiking quiescence1,2,4–6. Both cortical7–10 and thalamic11–15 origins have been proposed for the generation of cortical UP-states. For instance, isolated cortical circuits spontaneously produce UP- and Down-states7,16 and a subset of layer V 'pacemaker' neurons can recruit larger ensembles of pyramidal neurons to induce UP-states *in vitro*10. On the other hand, pharmacological inactivation of sensory thalamic neurons12,13 or cortical de-afferentiation (i.e., from thalamic, but also brainstem, inputs) inhibits local UP-state initiation in rodents and cats2,13,14. Considering that slow waves in the deafferented cortex have different dynamics (e.g.: lower frequencies and prolonged Down-state duration) than ones recording from intact brain tissue7,8, together these studies suggest a contribution of the thalamus to the temporal coordination of cortical slow waves during sleep.

Current understanding of the synaptic and cellular mechanisms underlying cortical slow waves stems primarily from investigations into sensory thalamocortical circuits1,2,6,16. However, the cortical heterogeneity17,18, prefrontal cortex origin19 and brain-wide travelling20 of cortical slow waves suggest the involvement of non-sensory, in particular midline and higher order, thalamic nuclei. Indeed, excitatory drive from the midline thalamus has emerged as an essential hub for control of cortical excitability21,22, NREM sleep consolidation23 and consciousness24, however, its precise role in sleep-wake control remains unclear.

We reasoned that midline thalamus neurons may play an important role in pacing cortical UP-states during sleep and possibly wakefulness. The mammalian midline thalamus consists of five nuclei that receive extensive input from the brainstem - including from adrenergic, cholinergic and serotonergic neurons25,26 - and from the hypothalamus27, hippocampus28 and prefrontal cortex29. In turn, they project to the cingulate (CING) and insular cortex, as well as the amygdala, zona incerta (ZI) and striatum29,30. We therefore investigated the role of midline thalamus neurons in the control of cortical UP-states during NREM sleep, sleep-wake behavioral transitions and sleep recovery using multisite tetrode recordings and optogenetic perturbation in freely behaving mice. We found that burst firing of centromedial thalamus (CMT) neurons controls the onset of CING UP-states while their tonic firing triggers awakening from NREM sleep. Furthermore, we show that brain-wide synchrony of cortical UP-states is dependent on a higher-order thalamic relay and promotes sleep recovery. Together, our findings identify a dual role for medial and dorsal thalamic neuron firing in both sleep and wake states.

Results

CMT neurons are phase advanced to the cortical UP-state

First, to identify the temporal dynamics of neuron firing from distinct midline thalamic nuclei, we simultaneously recorded the electroencephalogram (EEG), electromyogram (EMG), local field-potentials (LFPs) and unit activity using linear array electrodes across spontaneous sleep-wake states in freely moving wild-type mice (see Online Methods; Fig.

1a, b; Supplementary Fig. 1). Interestingly, we found that CMT neuron activity was significantly phase-advanced to the onset of the UP-state underlying the slow-wave in CING during NREM (as measured by the half-time of sigmoidal fits of their neuronal spiking activity at the onset of the cortical UP-state), as compared to all other neurons from the midline nuclei (CMT *vs* reuniens, rhomboideus (RHO), intermediodorsal (IMD), and paraventricular, $P = 0.0073$; $f = 4.422$; d.f. = 4; $n = 22, 23, 7, 28$ and 8 cells, respectively, $n = 6$ animals; one-way ANOVA; Fig. 1c, d, Supplementary Table 1; Supplementary Table 2).

The non-overlapping connectivity map between the midline and lateral (sensory) thalami suggests distinct functions in cortical control and sleep. To discriminate between these two regions in the control of local UP-states in CING and global arousal, we compared neuron spiking activity concurrently in the CMT and ventrobasal complex (VB; CMT: $n = 8$; VB: $n = 8$ cells; $n = 6$ animals) using multi-site tetrode recordings (see Online Methods; Fig. 2a). Both CMT and VB neuron spike rates were strongly modulated across sleep-wake states with high activity during rapid eye movement sleep (REM) (CMT: 25.9 ± 1.6 spike/s; VB: 35.3 ± 4.1 spikes/s; $P = 0.0087$; $t = 4.55$; d.f. = 5; one-sided *t*-test) compared to Wake (CMT: 6.3 ± 0.5 spikes/s; VB: 14.7 ± 2.9 spikes/s; $P = 0.032$; $t = 3.71$; d.f. = 5; one-sided *t*-test) and NREM (CMT: 4.6 ± 1.2 spikes/s; VB: 7.5 ± 0.9 spikes/s; $P = 0.041$; $t = 3.00$; d.f. = 5; one-sided *t*-test; Fig. 2b; Supplementary Table 1; Supplementary Table 2). Inter-spike interval analysis revealed a predominant bursting pattern of neuron firing in both CMT and VB during NREM (Peak inter-spike interval: Wake: CMT: 19.8 ± 6.4 ms; VB: 14.3 ± 5.2 ms; NREM: CMT: 11.1 ± 1.5 ms; VB: 8.9 ± 2.2 ms; REM: CMT: 15.4 ±3.2; VB: 13.6 ± 1.9; 2c, d). However, there was no coherence of spiking activity between CMT and VB cells to UP-Down-states (Peak inter-burst interval count CMT: 173.3 ± 8.3 ms; VB: 65.0 ± 8.9 ms; $P = 0.0064$; $t = 8.86$; d.f. = 10; two-sided *t*-test; Fig. 2e, f). Importantly, spike timing of CMT neurons followed a faithful rhythmicity in advance of the cortical UP-state ($t_{½} = -48.79$ ± 12.5 ms, $P < 0.01$; $t = 4.52$; d.f. = 5; one-sided *t*-test; Fig. 2g) and was also advanced relative to VB neurons ($t_{½} = +6.9 \pm 28.4$ ms; $P = 0.0008$; $t = 9.7$; d.f. = 6; one-sided *t*-test; Fig. 2g, i).

CMT neurons are phase-advanced to behavioral/sleep-wake transitions

Previous investigations of thalamic control of cortical state have focused on primary sensory thalamocortical ‘loops’16, however others have suggested different roles for midline and sensory thalamus in sleep-wake control31, attention and consciousness24,32. Thus, in the present study, we aimed to compare the cellular activity from thalamic nuclei of different modalities, namely arousal/attention (CMT), sensory (VB) and higher order thalami across sleep-wake states. In agreement with the phase advancement of CMT over VB neurons at the onset of cortical UP-states, we showed that CMT neuron spiking rates were also advanced over VB neurons during global NREM-to-Wake transitions (NREM-to-Wake: CMT: -9.2 ± 2.9 ms; VB: 25.9 ± 8.2 ms; $P = 0.027$; $t = 6.39$; d.f. = 6; Wake-to-NREM: CMT: -54.8 ± 14.2 ms; VB: 5.6 ± 6.2 ms; $P = 0.0051$, $t = 4.16$; d.f. = 6; two-sided *t*-test; Fig. 2h, j; Supplementary Fig. 2). Note that immediately after awakening, CMT and VB neuron spike rates both increased significantly above that seen during wake maintenance and returned to baseline values after ca. 10 s of wakefulness (Fig 2h, bottom panel). Collectively,

these results show that CMT and VB neurons are differentially modulated across sleep-wake states, suggesting distinct functions in controlling cortical excitability.

Activation of CMT but not VB neurons induces rapid wakefulness

Given the phase advancement of the CMT over central and lateral (VB) thalamic neurons during sleep-wake transitions, we tested whether optogenetic activation of CMT neurons induced awakening from natural sleep. To assess this, we targeted the expression of channelrhodopsin (*ChR2-EYFP*) to excitatory cells in the CMT or VB of wild type mice using stereotactic injection of a *CamKII-ChR2-EYFP* or *CamKII-EYFP* (control) adeno-associated virus 2 (AAV2; see Methods; Fig. 3a; Supplementary Fig. 3). We then optogenetically activated these areas at a range of frequencies (5-20 Hz; 473nm) 10 s after the onset of NREM (Fig. 3a, b; Supplementary Fig. 4, 5 for fidelity responses; See Online Methods and REF [3]). We found that optogenetic activation of *ChR2-EYFP*-expressing CMT neurons produced rapid awakening (see Methods) from NREM at all frequencies tested, as compared to control conditions (Latencies to awakening: 5 Hz: $P = 0.00008$; $t = 26.75$; d.f. = 10; 20 Hz: $P = 0.00006$; $t = 41.68$; d.f. = 10; 1 s: $P = 0.00006$; $t = 27.23$; d.f. = 10; two-sided t-test; ChR2: $n = 6$ animals; EYFP = 6 animals; Fig. 3b, c, Supplementary Table 3), whereas bilateral optogenetic activations of VB neurons did not (5 Hz: $P = 0.23$; $t = 2.19$; d.f. = 10; 20 Hz: $P = 0.51$; $t = 0.63$; d.f. = 10; 1 s: $P = 0.46$; $t = 1.75$; d.f. = 10; two-sided t-test; ChR2: $n = 6$ animals; EYFP = 6 animals; Fig. 3b, d). Single light-pulse activation of CMT neurons increased the likelihood of NREM–wake transitions in a stimulus-duration-dependent manner (ED_{50} of 255 ± 23.7 ms; $n = 6$ animals; Fig. 3e).

To identify the circuitry involved in CMT neuron induced awakening, we mapped the CMT efferents using ChR2-assisted mapping by targeting the expression of *ChR2-EYFP* to excitatory cells in the CMT neurons of wild type mice stereotactically injected with a *CamKII-ChR2-EYFP* AAV2 (see Online Methods; Supplementary Fig. 3). Consistent with previous studies29, axonal projections to cortical areas were restricted to CING and insular cortices, while few subcortical terminals were found in the striatum, amygdala and ZI (Supplementary Fig. 3). No retrogradely labelled cell bodies were found distant from the injection site.

We further showed that optogenetic activation of *ChR2-EYFP*-expressing CMT axon terminals in CING during NREM recapitulated the rapid wakening seen upon CMT cell body activation ($P = 0.00013$; $f = 2567$; d.f. = 2; two-way ANOVA; See Online Methods; $n = 5$ animals; Fig. 3f), while no changes were observed upon activation of insular cortex or ZI ($P > 0.05$; insular cortex: $n = 5$ animals; ZI: $n = 5$ animals; Fig. 3g, h; Supplementary Table 3). Light stimulation of CING in non-transfected control animals did not hasten awakening (5 Hz: 54.1 ± 1.6 s, 20 Hz: 55.3 ± 1.7 1 s: 54.0 ± 1.3; CING-control vs. Insular or ZI: $P > 0.05$; one-sided t-test; $n = 6$ animals; Supplementary Table 3). Interestingly, layer 5 neurons in CING showed a high-fidelity response to 1, 5 and 20-Hz trains of optical stimulation of *ChR2-EYFP*-expressing CMT neurons (Supplementary Fig. 4). Optogenetic activation of *ChR2-EYFP*-expressing VB neurons elicited responses only in barrel cortex (BARR) and did not alter CING neuronal activity (Supplementary Fig. 5).

These results show that tonic firing duration, rather than frequency, of CMT neuron activity controls NREM–wake transitions, while VB neurons seem to have a minimal involvement in sleep-wake state control.

Brain-wide synchronization of CMT neuron-induced UP-like states are dependent on a dorsal thalamic relay

CMT neuron firing was phase-advanced to cortical UP-states (Fig 2). This raises the question whether CMT neurons actually contribute to the initiation of UP-states and, if so, through what neural circuit. Consistent with previous studies29,30, we found no CMT neuron projections in posterior neocortical areas, other areas of the thalamus (except the ZI) or in the brainstem (Supplementary Fig. 3), leaving the possibility for either a cortico-cortical or a cortico-thalamic-cortical33 spreading of excitatory signals supporting the propagation of UP-states19. To test for the presence of a thalamic relay, we first mapped CING neuron efferents by targeting the expression of *ChR2-mCherry* to excitatory cells in the CING (layer 5) of wild type mice by stereotactic injection of a *CamKII-ChR2-mCherry* AAV2 in the same anterior-posterior segment as we had found afferents from CMT neurons (see Online Methods; Supplementary Fig. 6).

We found sparse short-range cortical projections to M1 area and diffuse low intensity projections throughout most of the lateral and reticular thalamic nuclei, suggesting that propagation of activity from the CMT-CING network may reach distant cortices via an indirect thalamic route (Supplementary Fig. 6). Indeed, the densest terminals were observed in the antero-dorsal nucleus of the thalamus (AD; Supplementary Fig. 6), suggesting a relay function for those cells. Unlike CMT cells, AD neurons have broad cortical projections34, and therefore represent a potential candidate for initiating widespread cortical UP-states. Supporting this, we mapped AD efferents by targeting the expression of archeorhodopsin (*ArchT-EYFP*) to excitatory cells in AD of wild type mice stereotactically injected with a *CamKII-ArchT-EYFP* AAV2 and found extensive ipsilateral projections, possibly via an axonal tract ventral to the laterodorsal thalamus, across most areas of the posterior cortex in both layers 1 and 4, including the visual cortex (VIS), as well as the retrosplenial cortex as shown previously34 (Supplementary Fig. 7).

To demonstrate the relay nature of AD neurons within the CMT-CING-AD-VIS circuit, we used a combinatorial optogenetic approach by targeting expression of ChR2 and ArchT to excitatory CMT and AD neurons using stereotactic injection of *CamKII-ChR2-EYFP* and *CamKII-ArchT-EYFP* AAV2, respectively. Optical fibers were chronically implanted dorsal to the CMT and AD areas and neuron activity/LFPs were simultaneously recorded from CMT, AD, CING (layer 5), BARR (layer 5) and VIS (layer 5) areas using multi-site tetrode recordings in freely-moving animals (see Online Methods; Fig. 4a, b). We recorded neurons in layer 5 since it is the proposed site of cortically generated slow oscillations and the locus of cortico-fugal projections10. We first found that CMT, CING, AD, BARR and VIS spiking rates were all modulated across sleep-wake states (Supplementary Fig. 8; Supplementary Table 1).

Confirming our initial findings (Fig.1), phase-locking values - determined from the half-times ($t_{1/2}$) of sigmoidal curve fits - indicated that a CMT-CING network may initiate

cortical UP-states (CMT: $P < 0.01$; $t = 4.30$; d.f. = 7; $n = 9$ cells; CING: $P < 0.05$; $t = 4.08$; d.f. = 7; one-sided *t*-test; $n = 8$ cells; $n = 6$ animals; Supplementary Fig. 8; Supplementary Table 1), as has been suggested based on recordings in anesthetized rats31. We showed that optogenetic burst-*like* activation of *ChR2-EYFP*-expressing CMT neurons consistently induced UP-*like* states in the CING cortex (Fig 4c, d; Supplementary Fig. 9; Supplementary Table 1; Supplementary Table 2). We found no difference between spontaneous or optogenetically induced slow-wave activity, as measured by average duration of UP and Down-states in CING (Fig. 4e-g; UP: $P = 0.45$; $t = 0.87$; d.f. = 7; Down: $P = 0.56$; $t = 0.66$s; d.f. = 7; two-sided *t*-test; $n = 8$ animals). Importantly, temporal lags of UP-*like* states between CMT, CING, AD and VIS cells suggested a serial, rather than parallel, pathway (CMT-to-CING: $P < 0.00009$; $t = 9.18$; d.f. = 8; CING -to-AD: $P = 0.000017$; $t = 22.35$; d.f. = 8; AD-to-BARR: $P = 0.0068$; $t = 3.621$; d.f. = 8; AD-to-VIS: $P = 0.0094$; $t = 7.18$; d.f. = 8; BARR-to-VIS: $P = 0.64$; $t = 0.49$; d.f. = 8; one-sided *t*-test; Figure 4h; Supplementary Table 1). To further confirm this finding, we showed that optogenetic silencing of *ArchT-EYFP*-expressing AD neurons completely prevented the induction of UP-*like* states in VIS neurons by optogenetic driving of *ChR2-EYFP*-expressing CMT neurons (Fig. 4d). Consistent with the low coherence between midline and lateral sensory thalamic circuit activity, UP-*like* states in BARR were minimally affected by CMT neuron activation and AD neuron silencing in this experiment (Fig. 4d; Supplementary Fig. 4). Interestingly, note that unilateral optical silencing of AD significantly prolonged the duration of NREM episode duration (Supplementary Fig. 10).

To determine the contributions of each hub of the CMT-CING-AD-VIS network, we targeted expression of *ArchT-EYFP* to excitatory neurons of CMT, CING and AD in separate cohorts of animals, by stereotactic injection of *CamKII-ArchT-EYFP* or *CamKII-EYFP* AAV2 (control) and optogenetically silencing *ArchT-EYFP*-expressing neurons during NREM sleep (Fig. 5a, b, j, o). Consistent with our optogenetic activation results, silencing of *ArchT-EYFP*-expressing CMT neurons decreased synchrony (as measured by the slope of modulation and the onset of cortical UP-state) in layer 5 CING and VIS neurons, but not layer 5 BARR cortex neurons (CING: $P = 0.008$; $t = 2.66$; d.f. = 16; $n = 9$ cells; BARR: P = 0.96; $t = 0.05$, d.f. = 10; $n = 6$ cells; VIS: $P = 0.002$; $t = 3.87$; d.f. = 14; $n = 8$ cells; from $n = 6$ animals; two-sided *t*-test; Fig. 5c-f). Interestingly, optogenetic silencing of CMT neurons also reduced phase synchrony between CMT, CING, AD and VIS in *ArchT-EYFP*-expressing animals compared to controls (Fig. 5g, h). This was accompanied by a decrease of CING slow wave power ($P = 0.008$; $t = 4.809$, d.f. = 5; Fig. 5i) that was consistently followed by a rebound in cortical slow wave power ($P = 0.005$; two-sided *t*-test; $t = 5.02$; d.f. = 5; $n = 6$ animals; Fig. 5i).

We further found that optogenetic silencing of CING neurons reduced synchrony in VIS neurons ($P = 0.014$; two-sided *t*-test; $t = 3.99$, d.f. = 4) but not BARR neurons ($P = 0.86$; $t = 1.02$; d.f. = 4; two-sided *t*-test; Fig. 5j-m; $n = 6$ cells; from $n = 5$ animals) and decreased normalized slow-wave power in VIS ($P = 0.036$; one-sided *t*-test; $t = 3.99$; d.f. = 3, from $n = 5$ animals; Fig. 5n). Accordingly, we found that optogenetic silencing of *ArchT-EYFP*-expressing CING neurons completely prevented the induction of UP-*like* states in AD and VIS cortical neurons by optogenetic driving of *ChR2-EYFP*-expressing CMT neurons (Supplementary Fig. 9). Similarly, optogenetic silencing of AD neurons reduced synchrony

in VIS neurons ($P = 0.036$; two-sided *t*-test; $t = 6.84$, d.f. = 8; $n = 10$ cells) but not BARR neurons ($P = 0.75$; $n = 9$ cells; from $n = 6$ animals; Fig. 5o-r) and decreased normalized slow-wave power in VIS ($P = 0.011$; $t = 4.63$; d.f. = 4; from $n = 6$ animals; one-sided *t*-test; Fig. 5s). Optogenetic silencing did not induce awakening.

In accordance with the proposed role of the CMT in generating cortical UP-states, UP-*like* states induced by burst-*like* optogenetic stimulation of CMT neurons (Fig. 6a, b) resulted in increased firing synchrony in CING and VIS across cortical UP-states (CING: $P = 0.004$; $t = 3.29$; d.f. = 16; $n = 8$ cells; BARR: $P = 0.62$; $t = 0.51$, d.f. = 12; $n = 6$ cells; VIS: $P = 0.013$; $t = 2.58$; d.f. = 14; two-sided *t*-test; $n = 7$ cells; from $n = 6$ animals; Fig. 6c-f, Supplementary Fig. 9). This was accompanied by an increased phase synchrony between CMT, CING, AD and VIS in *ChR2-EYFP*-expressing animals compared to controls (Fig. 6g, h). We further found a significant increase in CING slow-wave power ($P = 0.0006$; $t = 7.59$; d.f. = 5; two-sided *t*-test; $n = 6$ animals; Fig. 6i). Optogenetically-evoked UP-*like* states during NREM did not induce awakening. These results suggest that CMT neurons contribute to the initiation of UP-states in CING which propagate to VIS via AD relay cells. Note that this does not take account of isolated cortical slow waves originating in parietal or occipital cortices18,19.

CMT neuron activity promotes sleep recovery

During sleep recovery following a period of sleep deprivation, slow-wave power and cortical synchrony are increased18,35, as a measure of sleep pressure. In this context, travelling of slow waves has been suggested to promote sleep19, however direct involvement of medio-dorsal thalamo-cortical networks in sleep recovery has yet to be investigated. We therefore investigated the thalamic contribution to sleep recovery. We measured LFPs and spiking activity during sleep recovery following 4-hour sleep deprivation in freely moving mice (see Online Methods; Fig. 7a). During spontaneous recovery sleep, we found that slow-wave power (normalized to power during baseline sleep) was significantly increased in the CMT (2.0 ± 0.3; $P < 0.05$; $t = 3.7$; d.f. = 4), CING (2.7 ± 0.4; $P > 0.05$; $t = 4.1$; d.f. = 4), AD (2.7 ± 0.5; $P < 0.05$; $t = 3.5$; d.f. = 4) and VIS (2.3 ± 0.3; $P < 0.05$; $t = 3.9$; d.f. = 4), however, it was not significantly increased in BARR (1.0 ± 0.1; $P < 0.05$; $t = 0.6$; d.f. = 4; $n = 6$ animals; one-sided *t*-test; Supplementary Fig. 11, *see* below and discussion). Consistent with this finding, we found a significantly increased synchrony of neuron spiking, revealed by the slope of their curve fits at the onset of the cortical UP-state18, within CMT ($P < 0.05$; $t = 4.12$; d.f. = 12),CING ($P < 0.05$; $t = 4.36$; d.f. = 14), AD ($P < 0.05$; $t = 4.78$; d.f. = 14) and VIS ($P < 0.05$; $t = 4.53$; d.f. = 14; one-sided *t*-test) during sleep recovery, but reduced for neurons in BARR ($P < 0.05$; $t = 4.11$; d.f. = 14; Supplementary Table 1; Supplementary Fig. 11, 12). Interestingly, CMT neurons conserved their phase advancement over recorded cortical, midline and sensory thalamic neurons during sleep recovery (Supplementary Fig. 11, 12). Note that VB, but not CMT, LFPs recordings displayed sleep-*like* activity - i.e., large amplitude, low frequency oscillations – when animals were awake during the sleep deprivation procedure, as evidenced by the increased slow-wave power (Supplementary Fig. 12f, g).

To test whether perturbation of midline thalamus activity alters sleep recovery, we induced cortical slow-wave-*like* activity by burst-*like* optogenetic activation of CMT neurons and

measured the subsequent slow-wave power in CING during the sleep recovery following a 4-hour sleep deprivation (Fig. 7a lower panel). To exclude direct optogenetic network effects, quantification was conducted on NREM episodes where no optical stimulation was delivered (see Online Methods; Fig. 7a). We found that inducing slow-wave-*like* activity by optogenetic activation of *ChR2-EYFP*-expressing CMT neurons hastened the sleep recovery process, as measured by a faster reduction in slow-wave power and return to baseline levels ($P < 0.035$; $t = 4.59$; d.f. = 7; one-way ANOVA; $n = 6$ animals; Fig. 7b). In contrast, optogenetic silencing of *ArchT-EYFP*-expressing CMT neurons retarded the process ($P < 0.027$; $t = 3.86$; d.f. = 5; one-way ANOVA; $n = 6$ animals; Fig. 7c). Simultaneous optogenetic activation and silencing of CMT and AD neurons, respectively, resulted in no change from control animals (i.e.: no stimulation; $P = 0.25$; $t = 1.74$; d.f. = 5; one-way ANOVA; $n = 6$ animals; Fig. 7d). Finally, optogenetic silencing of CING neurons similarly delayed the sleep recovery process ($P = 0.013$; $t = 5.68$; d.f. = 4; one-way ANOVA; $n = 5$ animals; Fig. 7e). These results indicate that sleep recovery process is dependent on synchronized activity throughout the CMT-CING-AD-VIS circuit and the brain-wide propagation of slow waves.

Discussion

An intact midline thalamus is required for proper brain function during both wakefulness and sleep in rodents32 and humans24. Indeed, CMT damage is associated with disturbances of arousal, cognition and sleep23, whilst electrical stimulation of the midline thalamic nuclei, including the CMT, improves behavioral responsiveness in minimally-conscious patients24. CMT neurons are centrally positioned to contribute to cortical UP/DOWN-states, arousal and consciousness in the mammalian brain. Both the intrinsic and extrinsic control of CMT neuronal firing remains poorly understood, however, pharmacological activation of nicotinic acetylcholine receptors and inhibition of potassium channels in the CMT both cause emergence from anesthesia in rats32. This effect was not observed with activation of other midline thalamic nuclei. Together with our results this suggests that the CMT is a strong modulator of cortical arousal, although whether other midline thalamic nuclei can cause cortical activation remains to be investigated. CMT neurons receive inputs from adrenergic, serotonergic25, gabaergic27 and cholinergic36 neurons. Unlike dorsal and sensory thalamic neurones37, they are more susceptible to depolarization by external inputs originating from sub-cortical areas, since they do not possess the hyperpolarization activated (I_h) current. Altogether, this suggests that other intrinsic currents leave them susceptible to synaptic inputs38. In turn, neurons from the midline thalamus, and the CMT in particular, have extensive projections to the frontal cortex and striatum29.

Here we demonstrate a dual-control function of excitatory CMT neurons over sleep slow waves and awakening from NREM sleep, depending on the firing pattern and duration of firing of CMT neurons. Optogenetic tonic activation of CMT neurons reliably induced rapid awakening from NREM when the duration of the optical stimulations was longer than 500 ms, while stimulation mimicking spontaneous burst firing triggered slow-wave-*like* activity and enhanced cortical synchrony but not awakening. During NREM, CMT neurons contribute to the initiation of cortical UP-states in the CING that are synchronized over brain-wide cortical circuits by thalamic AD relay cells; however, despite the accurate

anatomical location of our recording sites, genetic targeting of opsin expression extended beyond the anatomical boundaries of CMT and AD (i.e., RHO, IMD and latero-dorsal thalamus respectively), therefore, we cannot rule out some contribution of these structures in brain-wide synchronization. Our circuit supports the onset and synchrony of frontal cortical slow waves, however some isolated slow waves may also travel from posterior areas9 and propagate via cortico-cortical pathways19. These findings suggest that CMT and AD neurons precisely synchronize local17 and global10 cortical circuits and may therefore support cognitive processes during NREM sleep, such as slow-wave-dependent memory consolidation39. Indeed, neurodegeneration and low fMRI signals activity in AD are associated with high frequency EEG oscillations and less cortical synchronization and reduced amplitude of sleep slow waves40 in patients with schizophrenia41 and Alzheimer's disease42. Thus, hypo-activity of AD neurons impairs both the quality and quantity of sleep and may support learning and memory consolidation during sleep via anterior-posterior large-scale integration of information during consciousness43,44.

We propose that these frontally-generated cortical UP-states propagate along an "*N-type*" CMT-CING-AD-VIS (i.e., thalamo-cortico-thalamo-cortical) excitatory pathway that is distinct from classical thalamo-cortical "loops" in primary somatosensory feedback circuits (e.g., VB-BARR cortex loop)1,16. We propose that this pathway is important for long-range cortical synchrony of frontally-generated slow waves during NREM, sleep recovery and awakening from NREM through a poly-synaptic feedforward pathway, that is likely to involve local feedback circuits.

At the cortical level, our results are consistent with the frontal origin of cortical slow waves and their antero-posterior propagation in the mammalian brain19, as well as the minimal perturbations of cortical lesions on long-range neocortical connectivity33 and the confinement of traveling slow waves to the frontal cortex19,20. Our study provides evidence for an important contribution of the thalamus to the onset of cortical UP-states. The neocortex is capable of generating slow waves when thalamic inputs have been abolished2,7,45; however, the frequency of the oscillation is different between *in vivo* and *in vitro* preparations8 suggesting the importance of extrinsic inputs in the timing of the slow-wave generation. Furthermore, one investigation demonstrated that cortical slow-wave activity was transiently reduced during acute *in vivo* thalamic lesioning, recovering several days afterwards14, while other studies have demonstrated absence of effect of acute midline and intralaminar thalamus46 or chronic lesions45 on slow wave or fast cortical activity, suggesting the existence of extra-thalamic mechanisms that can support slow wave integrity, sleep-wake cycles and overall arousal. Collectively these data, together with the present study, implicate the midline and dorsal thalamus in the timing and synchrony of cortical slow waves in the healthy brain and provide an avenue for the investigation of NREM-sleep-dependent cognitive processes such as memory consolidation17.

During recovery sleep, the amplitude of cortical slow waves is correlated with increased synchrony of pyramidal neuron spiking18 (but see ref. 47). Our present data further implicate sub-cortical structures, in particular thalamic circuits, as previously suggested by the increased slow-wave activity upon disinhibition of RTN neurons in mice27. Consistent with this, the "*N-type*" circuit provides a network mechanism for the regulation of increased

Europe PMC Funders Author Manuscripts

cortical neuron spiking synchrony and emphasizes a role for midline and higher order thalamic neurons in the sleep recovery process. Within the somatosensory VB-BARR loop, the absence of increased slow-wave power during recovery sleep may reflect the sustained slow-wave activity during quiet sleep-deprived wakefulness, which may prevent the accumulation of sleep pressure. This latter observation further supports the distinct anatomical and functional role of midline and sensory thalamus in sleep control.

Interestingly, neurons from CMT and AD, as well as all cortical neurons recorded, showed highest discharge rates during REM sleep18. This may be due to strong cholinergic inputs from the laterodorsal tegmental nucleus to the midline thalamus48. These inputs, and the restricted projections of the medio-dorsal thalamus to insular and retrosplenial cortices and the adjacent claustrum49, suggest a role for the medio-dorsal thalamus in cortical processing of information during REM or consciousness during sleep as well as memory consolidation50, however, this remains to be experimentally investigated.

Collectively, our results further distinguish the anatomical and functional roles of midline and sensory thalamus during NREM sleep and strongly suggest that burst and tonic firing patterns of CMT neuronal firing exerts dual control of sleep slow waves and NREM–wake transitions, respectively. This implicates CMT and AD neurons in brain-wide synchronization of cortical activity, in particular the control of frontal and global cortical activity respectively, during sleep and sleep recovery.

Online Methods

Animals

We used C57Bl6 adult male mice (6 - 14 weeks old) from Charles Rivers Laboratories, Germany. Animals were housed in individual custom-designed polycarbonate cages at constant temperature (22 ± 1 °C), humidity (30 - 40 %), and circadian cycle (12-h light-dark cycle, lights on at 08:00). Food and water were available *ad libitum*. Animals were treated according to protocols and guidelines approved by the Veterinary Office of the Canton of Bern, Switzerland (License number BE 113/13). Animals were housed in IVC cages in groups of 2 - 5 before instrumentation and after virus injections. After implantation, all mice were housed individually. Animals were habituated to the recording cable and optical fibers in their open-top home cages (300 × 170 mm) and kept tethered for the duration of the experiments. Animals were allowed to move freely in the cage during *in vivo* electrophysiology experiments. Before commencing experimental recording, baseline sleep was recorded and compared to previously published results51 to confirm resumption of a normal sleep-wake cycle after instrumentation. Experiments were performed during the “lights-on” period (12:00 - 16:00). Viral injections were performed at 6 - 8 weeks of age and instrumentation at 10 - 12 weeks of age. All recordings were performed from 11 - 14 weeks of age. No animals were excluded from analysis.

Stereotaxic Injection of AAV

Six-week old C57Bl6 were anaesthetized in isoflurane (4.0 % for induction, 1.0-1.5 % for maintenance) in oxygen and mounted in a stereotaxic frame (Model 940, David Kopf

Instruments). Saline 10 ml/kg and meloxicam 5 mg/kg were given subcutaneously before incision. The skin on the head was shaved and aseptically prepared, and lidocaine 2 mg/kg infused subcutaneously at the incision site. A single longitudinal midline incision was made from the level of the lateral canthus of the eyes to the lambda skull suture. Injections were performed using a 28-gauge needle (Plastics One) connected by mineral oil filled tubing to a 10 μl Hamilton syringe in an infusion pump (Model 1200, Harvard Apparatus). Injections were performed at 0.1 μl/min and the needle left in situ for 10 minutes afterwards to allow diffusion. Injections were performed in CMT (AP -1.7 mm, ML +1.0 mm, DV -3.8 mm, 15°, 100 nl), AD (AP -0.9 mm, ML ± 0.8 mm, DV -3.2 mm, 150 nl) and CING (AP +1.8 mm, ML +0.2 mm, DV -1.6 mm, 100 nl). Co-ordinates based on the mouse brain atlas52. Animals were randomly assigned to receive either *AAV2-CamKII-E1fa-ChR2-EYFP* for optical stimulation, or *AAV2-CamKII-E1fa-EYFP* as control for direct retinal stimulation of CMT and VB. For experiments in Fig. 3c, d, animals were randomly assigned to receive injections in either CMT or VB. Silencing of AD or CING was achieved with *AAV2-CamKII-E1fa-ArchT3.0-EYFP* and *AAV2-CamKII-E1fa-ChR2-mCherry* was used for anatomical tracing of projections from the CING. All plasmids were obtained from University of North Carolina Vector Core Facility. Animals were left for three weeks before instrumentation or sacrifice for histology.

Instrumentation

Animals were anaesthetized by isoflurane in oxygen and mounted in a stereotaxic frame. Saline 10 ml/kg and meloxicam 5 mg/kg were given subcutaneously. The skin on the head was shaved and aseptically prepared, and lidocaine 2 mg/kg infused subcutaneously at the incision site. A single longitudinal midline incision was made from the level of the lateral canthus of the eyes to the lambda skull suture. Three stainless steel screws were placed in the skull to measure EEG (EEG: AP -2.3 mm, ML ±2.0 mm, REF: AP -4.3 mm, ML +0.5mm) and two bare-ended wires sutured to the trapezius muscle of the neck to record EMG. Tetrodes were made from 4 strands of 10 μm twisted tungsten wire (CFW0010954, California Fine Wire), connected to an electrode interface board by gold pins and were inserted into the CMT (AP -1.7 mm, ML +1.0 mm, DV -3.8 mm, 15°), CING (AP +1.8 mm, ML +0.2 mm, DV -1.6 mm), AD (AP -0.9 mm, ML ± 0.8 mm, DV -3.2 mm), BARR (AP -2.0 mm, ML +2.2 mm, DV -1.1 mm) and VIS (AP -3.3 mm, ML +2.5 mm, DV -0.9 mm) and secured to the skull with dental acrylic (C&B Metabond). Linear array electrodes (A1x16-5mm-100-177-CM16LP, Neuronexus) were implanted (AP -1.7 mm, ML ± 0.0 mm, DV -4.0 mm) to record from all midline thalamic nuclei (n = 6 animals). Optic fibers of 200 μm diameter were placed in the CMT (AP -1.7 mm, ML +1.0 mm, DV -3.8mm, 15°), bilaterally in VB (AP -1.7 mm, ML ±1.8 mm, DV -3.3 mm) and bilaterally in AD (AP -0.9 mm, ML ± 0.8 mm, DV -3.0 mm) and secured with the same dental acrylic. Optical stimulation of CMT axon terminals was performed with bilateral fibers in CING (AP +1.8 mm, ML ±0.2 mm, DV -1.3 mm), ZI (AP -0.9 mm, ML ±0.5 mm, DV -4.3 mm) and insular cortex (AP +0.5 mm, ML ±2.3 mm, DV -4.9 mm, 20°). For experiments in Fig. 3h, animals were randomly assigned to have optic fibers implanted in CING, ZI or insular cortex. Finally, the implant was stabilized using a methyl methacrylate cement and the animal allowed to recover in the home cage on top of a heating mat. Animals were allowed a minimum of 5 days to recover before starting recordings.

Data Acquisition

For experiments presented in Figure 3, mice were connected to a multichannel cable. EEG/EMG data was amplified (x1000) by an analogue amplifier (Model 3500, AM Systems) and digitized at 200 Hz via a digital-analogue converter (NIDAQ 6363, National Instruments). For all other recordings, mice were connected to a tethered digitizing headstage (RHD2132, Intan Technologies) and data sampled at 20 kHz recorded in free open source software (RHD2000 evaluation software, Intan Technologies). Optical fibers were connected to a patch chord using a zirconia sleeve (Doric Lenses). The patch chords were coated in black furcation tubing and connections covered in black varnish to prevent ocular stimulation from the laser. Habituation to the cables was performed up to 8 hours per day until the animals had nested and resumed a normal sleep-wake cycle. To ensure a correct sleep-wake cycle had been regained following instrumentation, we recorded a baseline of natural sleep from ZT 4 to 9 and compared the results to previously published works (Supplementary Fig. 1,27). All optogenetic experiments were performed between ZT 4 and 8. Optogenetic stimulation was performed with blue light (473 nm) from a laser (LRS-0473-PFM-00100-05, Laserglow Technologies) via a patch chord, 10s after the start of NREM, judged by an experienced experimenter in real time, as an appropriate latency to consider ongoing NREM sleep episodes as stable as described previously27,53. Optical inhibition was performed with green light (532 nm) from a laser (LRS-0532-GFM-00100-03, Laserglow Technologies) also via a patch chord. Laser output was controlled using TTL from a pulse generator (Master-9, AMPI or PulsePal 2, Sanworks). TTL signals were co-acquired with all recordings.

Awakening was assessed by an abrupt increase in EMG activation, often accompanied with movements, concurrent with cortical activation, typically assessed by increased frequency and decreased amplitude of the EEG, as previously reported by us27,53 and others54.

Signal Processing

Sleep scoring was performed manually based on frequency and amplitude characteristics of the EEG and EMG in custom software written in MATLAB using 1-s epochs to allow accurate tracking of microarousals55,56. We defined NREM as high amplitude synchronous activity in the EEG with a delta (1 - 4.5Hz) frequency dominating the signal and low EMG amplitude, REM as highly synchronous theta (5 - 10Hz) and flat EMG and wake as increased EMG activity. The start of wake was defined as the first epoch with a rapid increase in muscle tone concurrent with a low amplitude, fast frequency (> 6 Hz) EEG, NREM was defined as the epoch containing the first slow wave of more than 200μV amplitude, wake as the first epoch with a rapid increase in muscle tone, and REM as the epoch with a reduced EMG tone and consolidated theta:delta ratio more than 1. In cases where EEG/EMG was co-acquired with unit activity, data was down-sampled to 500 Hz before scoring sleep stages by applying a low pass filter (200 Hz, Chebyshev Type I, order 8, 0.05 dB passband ripple) to prevent aliasing. During scoring, the experimenter was blinded to the timing of any optogenetic manipulation but not to the conditions of the experiment.

Multiunit activity was first extracted from bandpass filtered recordings (600 - 4000 Hz, 4^{th} order elliptic filter, 0.1 dB passband ripple, -40 dB stopband attenuation). Filtering was

performed in both the forward and reverse directions. The detection threshold was set as 7.5 times the median of the absolute value of the filtered signal. The detected multiunit activity was then sorted using the WaveClus toolbox57 to obtain single units. Briefly, a 4-level Haar discrete wavelet transform (wavedec, MATLAB) was applied to the detected multiunit activity, and the 10 most discriminative wavelet coefficients were selected using the Kolmogorov-Smirnov test. Selected wavelet coefficients were subsequently sorted using the super-paramagnetic clustering, as described previously57, to obtain single units. Sorted spikes were visually inspected and clusters with a completely symmetric shape or an average firing rate less than 0.2 Hz were discarded from the analyses. Stage specific inter-spike interval (ISI) histograms were created for individual units using 1 ms bin width. For cortical recordings, neurons with average firing rates over 20 spikes/s were omitted from analysis as they were likely to be interneurons. Interneurons were excluded from analysis since VIP+ cells do not participate in cortical slow wave generation5 and could not be differentiated from SOM+ interneurons in our preparation.

Burst firing of single units was detected as a minimum of three consecutive action potentials with ISI less than 6 ms and preceded by a quiescent hyperpolarized state of at least 50 ms58. Inter-burst interval (IBI) was defined as distance between centers of two consecutive bursting activity during NREM episodes. IBI histograms during NREM sleep were created for individual units using 200 ms bin width.

To detect UP/Down states, LFP/EEG signals were first bandpass filtered (0.5 - 3Hz) using window-based finite impulse response filter (fir1, MATLAB), with an order equal to three cycles of low cut-off frequency, in forward and reverse direction to provide zero-phase distortion (filtfilt, MATLAB). Individual UP-Down states were detected from zero-crossing of filtered signals. The onset of UP-states was defined as zero-crossing from negative to positive. To secure our analysis, we excluded individual UP-Down states that were shorter than 200ms or had absolute amplitude less than 1 standard deviation from the mean.

For each unit, the average firing rate during vigilance state was calculated as the total number of action potentials during a state divided by total time spent in that state and reported as number per second (Hz). Mean firing rates during vigilance state transition were calculated by averaging firing rates across transitions using a non-overlapping moving window of 100 ms. Mean firing rates during transition from Down to UP states were calculated by averaging firing rates of all detected Down to UP transitions using a non-overlapping moving window of 10 ms. Mean firing rates were then fitted with a Boltzmann sigmoidal curve in GraphPad Prism using the following equation:

$$y = minimum + \frac{maximum - minimum}{1 + \frac{t_{1/2} - x}{slope}}$$

Where y equals the neuronal firing rate and x equals time. The half-times of the curves ($t_{1/2}$) used for comparison of lag and phase. The slopes of the curve fits at the half-time point were used as a measure of neuronal firing modulation and therefore synchrony18.

Power spectral density (PSD) was estimated using Welch's method (pwelch, MATLAB), using 8 s windows having 75 % overlap, with 0.5 Hz resolution. Delta power in a recording segment was calculated using a modified periodogram (bandpower, MATLAB), considering the estimated Welch's PSD in 0.5 - 4Hz. Delta power during optogenetic perturbations was estimated for 10 s recording segments of pre, during, and post perturbation. NREM delta power during recovery sleep was calculated using a moving window of 10 minutes having 50 % overlap and was normalized to the power in the same frequency bin during baseline sleep (i.e.: no sleep deprivation) for each animal. This normalization corrects for variations in recorded signals across animals, which are mainly the result of different electrode impedances.

Phase synchronization between each pair of thalamic and cortical LFP recordings during spontaneous and optogenetic perturbations of NREM sleep were estimated using mean phase coherence59. To measure delta phase coherence, LFP signals were first filtered in the delta range (0.5 - 4Hz) using a 6000^{th} order FIR filter (fir1, MATLAB) in both the forward and reverse directions. Afterward, the instantaneous phases of delta oscillations were estimated using the Hilbert transform. Delta phase coherence was obtained by averaging the instantaneous phase differences of two filtered signals that are projected onto a unit circle in the complex plane. The estimated measure falls within [0 1] interval, where zero and one indicate completely incoherent and coherent delta rhythms, respectively.

For averaging of data acquired from linear array electrodes, we normalized the recording spots across animals based in histological findings. Changes in spike timing were averaged across reference points (behavioral transitions or detected UP-states) and fitted with a Boltzmann sigmoidal curve (see above for equation). The slope and relative half-time of these curves was then extrapolated.

Synchrony was determined by the slope of neuron firing or LFPs at the onset of cortical UP-state, as previously described60.

Sleep Deprivation

Animals were moved from the home cage to a new cage with clean bedding, food and water and a novel red plastic object at 08:00 (ZT 0). Gentle handling was performed when animals were stationary to prevent sleep. Four hours later (ZT 4) they were returned to their original home cage and EEG/EMG and spike/LFP recordings were obtained between ZT 4 and 9.

Immunohistochemistry

Animals were deeply anaesthetized with 15 mg pentobarbital (i.p.) and the heart transfused with 20 ml ice cold heparinized PBS followed by 30 ml 4 % formalin. Brains were removed and post-fixed overnight in 4 % formalin. They were then cryoprotected in 40 % sucrose for 24 - 48 hours. Sections of 30 μm were cut in a cryostat. Free-floating sections were washed in PBS plus 0.1 % Triton X-100 (PBS-T) three times for 10 minutes each and then blocked by incubation with 4% bovine serum albumin in PBS-T for 1 hour. Free floating sections were incubated with primary antibodies for GFP (Life Technologies: A10262; 1:4000) for 24 - 48 hours at 4 °C. They were then washed in PBS-T, three times for 10 minutes each and

then incubated with secondary antibody (Abcam: AB96947, 1:500) for 1 hour at room temperature.

Confirmation of electrode placement was performed in brain sections stained with bis-Benzimide as a counter stain to the DIO that coated the electrodes. Briefly, free-floating brain slices were exposed to bis-Benzimide (1 ug/ml) in PBS for 15 minutes at room temperature. Three washes of 15 minutes each in PBS were then performed and slices then mounted on glass slides and allowed to dry. A cover slip was placed of the slices with a mounting medium and then imaged on a confocal fluorescent microscope.

Statistical Analysis

Matlab (MathWorks) and Prism 6 (GraphPad) were used for statistical analysis. No power calculations were performed to determine sample sizes, however similar sized cohorts were used in other relevant investigations27. Data were compared via one-way ANOVA, or *t*-test for parametric data with post-hoc Tukey's correction for multiple comparisons. Data distribution was assumed to be normal but this was not formally tested. Values in the text are reported as mean ± standard error mean (S.E.M.) unless reported otherwise. Figures were prepared in Adobe CS6 (Adobe).

Supplementary Material

Refer to Web version on PubMed Central for supplementary material.

Acknowledgments

We thank the Tidis laboratory members for their technical help and comments on a previous version of the manuscript. We thank M. Mameli, S. Brown and C. Bassetti for helpful comments on the manuscript. We thank the laboratory of H.-R. Widmer and the M.I.C. UNIBE Facility for the use of the microscopes. Optogenetic plasmids were kindly provided by K. Deisseroth (Stanford University) and E. Boyden (MIT). A.A. was supported by the Human Frontier Science Program (RGY0076/2012), Inselspital University Hospital, the University of Bern, Swiss National Science Foundation (156156) and the European Research Council (ERC-2016-COG-725850).

References

1. Steriade M, Nunez A, Amzica F. Intracellular analysis of relations between the slow (< 1 Hz) neocortical oscillation and other sleep rhythms of the electroencephalogram. J Neurosci. 1993; 13:3266–3283. [PubMed: 8340807]
2. Steriade M, Nunez A, Amzica F. A novel slow (< 1 Hz) oscillation of neocortical neurons in vivo: depolarizing and hyperpolarizing components. J Neurosci. 1993; 13:3252–3265. [PubMed: 8340806]
3. Nir Y, et al. Selective neuronal lapses precede human cognitive lapses following sleep deprivation. Nat Med. 2017; 23:1474–1480. [PubMed: 29106402]
4. Contreras D, Steriade M. Cellular basis of EEG slow rhythms: a study of dynamic corticothalamic relationships. J Neurosci. 1995; 15:604–622. [PubMed: 7823167]
5. Neske GT, Patrick SL, Connors BW. Contributions of diverse excitatory and inhibitory neurons to recurrent network activity in cerebral cortex. J Neurosci. 2015; 35:1089–1105. [PubMed: 25609625]
6. Zucca S, et al. An inhibitory gate for state transition in cortex. Elife. 2017; 6
7. Timofeev I, Grenier F, Bazhenov M, Sejnowski TJ, Steriade M. Origin of slow cortical oscillations in deafferented cortical slabs. Cereb Cortex. 2000; 10:1185–1199. [PubMed: 11073868]
8. Sanchez-Vives MV, McCormick DA. Cellular and network mechanisms of rhythmic recurrent activity in neocortex. Nat Neurosci. 2000; 3:1027–1034. [PubMed: 11017176]

9. Vyazovskiy VV, Faraguna U, Cirelli C, Tononi G. Triggering slow waves during NREM sleep in the rat by intracortical electrical stimulation: effects of sleep/wake history and background activity. J Neurophysiol. 2009; 101:1921–1931. [PubMed: 19164101]
10. Lorincz ML, et al. A Distinct Class of Slow (approximately 0.2-2 Hz) Intrinsically Bursting Layer 5 Pyramidal Neurons Determines UP/DOWN State Dynamics in the Neocortex. J Neurosci. 2015; 35:5442–5458. [PubMed: 25855163]
11. Steriade M, Contreras D, Curro Dossi R, Nunez A. The slow (< 1 Hz) oscillation in reticular thalamic and thalamocortical neurons: scenario of sleep rhythm generation in interacting thalamic and neocortical networks. J Neurosci. 1993; 13:3284–3299. [PubMed: 8340808]
12. Hughes SW, Cope DW, Blethyn KL, Crunelli V. Cellular mechanisms of the slow (<1 Hz) oscillation in thalamocortical neurons in vitro. Neuron. 2002; 33:947–958. [PubMed: 11906700]
13. David F, et al. Essential thalamic contribution to slow waves of natural sleep. J Neurosci. 2013; 33:19599–19610. [PubMed: 24336724]
14. Lemieux M, Chen JY, Lonjers P, Bazhenov M, Timofeev I. The impact of cortical deafferentation on the neocortical slow oscillation. J Neurosci. 2014; 34:5689–5703. [PubMed: 24741059]
15. Sheroziya M, Timofeev I. Global intracellular slow-wave dynamics of the thalamocortical system. J Neurosci. 2014; 34:8875–8893. [PubMed: 24966387]
16. Poulet JF, Fernandez LM, Crochet S, Petersen CC. Thalamic control of cortical states. Nat Neurosci. 2012; 15:370–372. [PubMed: 22267163]
17. Huber R, Ghilardi MF, Massimini M, Tononi G. Local sleep and learning. Nature. 2004; 430:78–81. [PubMed: 15184907]
18. Vyazovskiy VV, et al. Cortical firing and sleep homeostasis. Neuron. 2009; 63:865–878. [PubMed: 19778514]
19. Massimini M, Huber R, Ferrarelli F, Hill S, Tononi G. The sleep slow oscillation as a traveling wave. J Neurosci. 2004; 24:6862–6870. [PubMed: 15295020]
20. Nir Y, et al. Regional slow waves and spindles in human sleep. Neuron. 2011; 70:153–169. [PubMed: 21482364]
21. Giber K, et al. A subcortical inhibitory signal for behavioral arrest in the thalamus. Nat Neurosci. 2015; 18:562–568. [PubMed: 25706472]
22. Liu J, et al. Frequency-selective control of cortical and subcortical networks by central thalamus. Elife. 2015; 4
23. Bassetti C, Mathis J, Gugger M, Lovblad KO, Hess CW. Hypersomnia following paramedian thalamic stroke: a report of 12 patients. Ann Neurol. 1996; 39:471–480. [PubMed: 8619525]
24. Schiff ND, et al. Behavioural improvements with thalamic stimulation after severe traumatic brain injury. Nature. 2007; 448:600–603. [PubMed: 17671503]
25. Royce GJ, Bromley S, Gracco C. Subcortical projections to the centromedian and parafascicular thalamic nuclei in the cat. J Comp Neurol. 1991; 306:129–155. [PubMed: 2040725]
26. Krout KE, Belzer RE, Loewy AD. Brainstem projections to midline and intralaminar thalamic nuclei of the rat. J Comp Neurol. 2002; 448:53–101. [PubMed: 12012375]
27. Herrera CG, et al. Hypothalamic feedforward inhibition of thalamocortical network controls arousal and consciousness. Nat Neurosci. 2016; 19:290–298. [PubMed: 26691833]
28. McKenna JT, Vertes RP. Afferent projections to nucleus reuniens of the thalamus. J Comp Neurol. 2004; 480:115–142. [PubMed: 15514932]
29. Vertes RP, Hoover WB, Rodriguez JJ. Projections of the central medial nucleus of the thalamus in the rat: node in cortical, striatal and limbic forebrain circuitry. Neuroscience. 2012; 219:120–136. [PubMed: 22575585]
30. Van der Werf YD, Witter MP, Groenewegen HJ. The intralaminar and midline nuclei of the thalamus. Anatomical and functional evidence for participation in processes of arousal and awareness. Brain Res Brain Res Rev. 2002; 39:107–140. [PubMed: 12423763]
31. Baker R, et al. Altered activity in the central medial thalamus precedes changes in the neocortex during transitions into both sleep and propofol anesthesia. J Neurosci. 2014; 34:13326–13335. [PubMed: 25274812]

32. Lioudyno MI, et al. Shaker-related potassium channels in the central medial nucleus of the thalamus are important molecular targets for arousal suppression by volatile general anesthetics. J Neurosci. 2013; 33:16310–16322. [PubMed: 24107962]
33. Contreras D, Destexhe A, Sejnowski TJ, Steriade M. Control of spatiotemporal coherence of a thalamic oscillation by corticothalamic feedback. Science. 1996; 274:771–774. [PubMed: 8864114]
34. Van Groen T, Wyss JM. Projections from the anterodorsal and anteroventral nucleus of the thalamus to the limbic cortex in the rat. J Comp Neurol. 1995; 358:584–604. [PubMed: 7593752]
35. Borbely AA. A two process model of sleep regulation. Hum Neurobiol. 1982; 1:195–204. [PubMed: 7185792]
36. Alkire MT, McReynolds JR, Hahn EL, Trivedi AN. Thalamic microinjection of nicotine reverses sevoflurane-induced loss of righting reflex in the rat. Anesthesiology. 2007; 107:264–272. [PubMed: 17667571]
37. McCormick DA, Pape HC. Properties of a hyperpolarization-activated cation current and its role in rhythmic oscillation in thalamic relay neurones. J Physiol. 1990; 431:291–318. [PubMed: 1712843]
38. Jhangiani-Jashanmal I, Yamamoto R, Gungor NZ, Pare D. Electroresponsive properties of rat central medial thalamic neurons. J Neurophysiol. 2016
39. Molle M, Bergmann TO, Marshall L, Born J. Fast and slow spindles during the sleep slow oscillation: disparate coalescence and engagement in memory processing. Sleep. 2011; 34:1411–1421. [PubMed: 21966073]
40. Wulff K, Gatti S, Wettstein JG, Foster RG. Sleep and circadian rhythm disruption in psychiatric and neurodegenerative disease. Nat Rev Neurosci. 2010; 11:589–599. [PubMed: 20631712]
41. Uhlhaas PJ, Singer W. Abnormal neural oscillations and synchrony in schizophrenia. Nat Rev Neurosci. 2010; 11:100–113. [PubMed: 20087360]
42. Zarei M, et al. Combining shape and connectivity analysis: an MRI study of thalamic degeneration in Alzheimer's disease. Neuroimage. 2010; 49:1–8. [PubMed: 19744568]
43. Kinomura S, Larsson J, Gulyas B, Roland PE. Activation by attention of the human reticular formation and thalamic intralaminar nuclei. Science. 1996; 271:512–515. [PubMed: 8560267]
44. Schmitt LI, et al. Thalamic amplification of cortical connectivity sustains attentional control. Nature. 2017
45. Fuller PM, Sherman D, Pedersen NP, Saper CB, Lu J. Reassessment of the structural basis of the ascending arousal system. J Comp Neurol. 2011; 519:933–956. [PubMed: 21280045]
46. Anaclet C, et al. Basal forebrain control of wakefulness and cortical rhythms. Nat Commun. 2015; 6:8744. [PubMed: 26524973]
47. Rodriguez AV, et al. Why Does Sleep Slow-Wave Activity Increase After Extended Wake? Assessing the Effects of Increased Cortical Firing During Wake and Sleep. J Neurosci. 2016; 36:12436–12447. [PubMed: 27927960]
48. Steriade M, Datta S, Pare D, Oakson G, Curro Dossi RC. Neuronal activities in brain-stem cholinergic nuclei related to tonic activation processes in thalamocortical systems. J Neurosci. 1990; 10:2541–2559. [PubMed: 2388079]
49. Shibata H, Honda Y. Thalamocortical projections of the anterodorsal thalamic nucleus in the rabbit. J Comp Neurol. 2012; 520:2647–2656. [PubMed: 22314639]
50. Boyce R, Glasgow SD, Williams S, Adamantidis A. Causal evidence for the role of REM sleep theta rhythm in contextual memory consolidation. Science. 2016; 352:812–816. [PubMed: 27174984]
51. Jego S, et al. Optogenetic identification of a rapid eye movement sleep modulatory circuit in the hypothalamus. Nat Neurosci. 2013; 16:1637–1643. [PubMed: 24056699]
52. Paxinos, G, Franklin, KBJ. Paxinos and Franklin's the Mouse Brain in Stereotaxic Coordinates. 4th Edition. Elsevier; 2012.
53. Adamantidis AR, Zhang F, Aravanis AM, Deisseroth K, De Lecea L. Neural substrates of awakening probed with optogenetic control of hypocretin neurons. Nature. 2007; 450:420–U429. [PubMed: 17943086]

54. Kroeger D, et al. Cholinergic, Glutamatergic, and GABAergic Neurons of the Pedunculopontine Tegmental Nucleus Have Distinct Effects on Sleep/Wake Behavior in Mice. J Neurosci. 2017; 37:1352–1366. [PubMed: 28039375]

55. McShane BB, et al. Characterization of the bout durations of sleep and wakefulness. J Neurosci Methods. 2010; 193:321–333. [PubMed: 20817037]

56. Morairty SR, et al. A role for cortical nNOS/NK1 neurons in coupling homeostatic sleep drive to EEG slow wave activity. Proceedings of the National Academy of Sciences. 2013; 110:20272–20277.

57. Quiroga RQ, Nadasdy Z, Ben-Shaul Y. Unsupervised spike detection and sorting with wavelets and superparamagnetic clustering. Neural Comput. 2004; 16:1661–1687. [PubMed: 15228749]

58. Guido W, Lu SM, Sherman SM. Relative contributions of burst and tonic responses to the receptive field properties of lateral geniculate neurons in the cat. J Neurophysiol. 1992; 68:2199–2211. [PubMed: 1491266]

59. Mormann F, Lehnertz K, David P, Elger CE. Mean phase coherence as a measure for phase synchronization and its application to the EEG of epilepsy patients. Physica D: Nonlinear Phenomena. 2000; 144:358–369.

60. Fattinger S, Jenni OG, Schmitt B, Achermann P, Huber R. Overnight changes in the slope of sleep slow waves during infancy. Sleep. 2014; 37:245–253. [PubMed: 24497653]

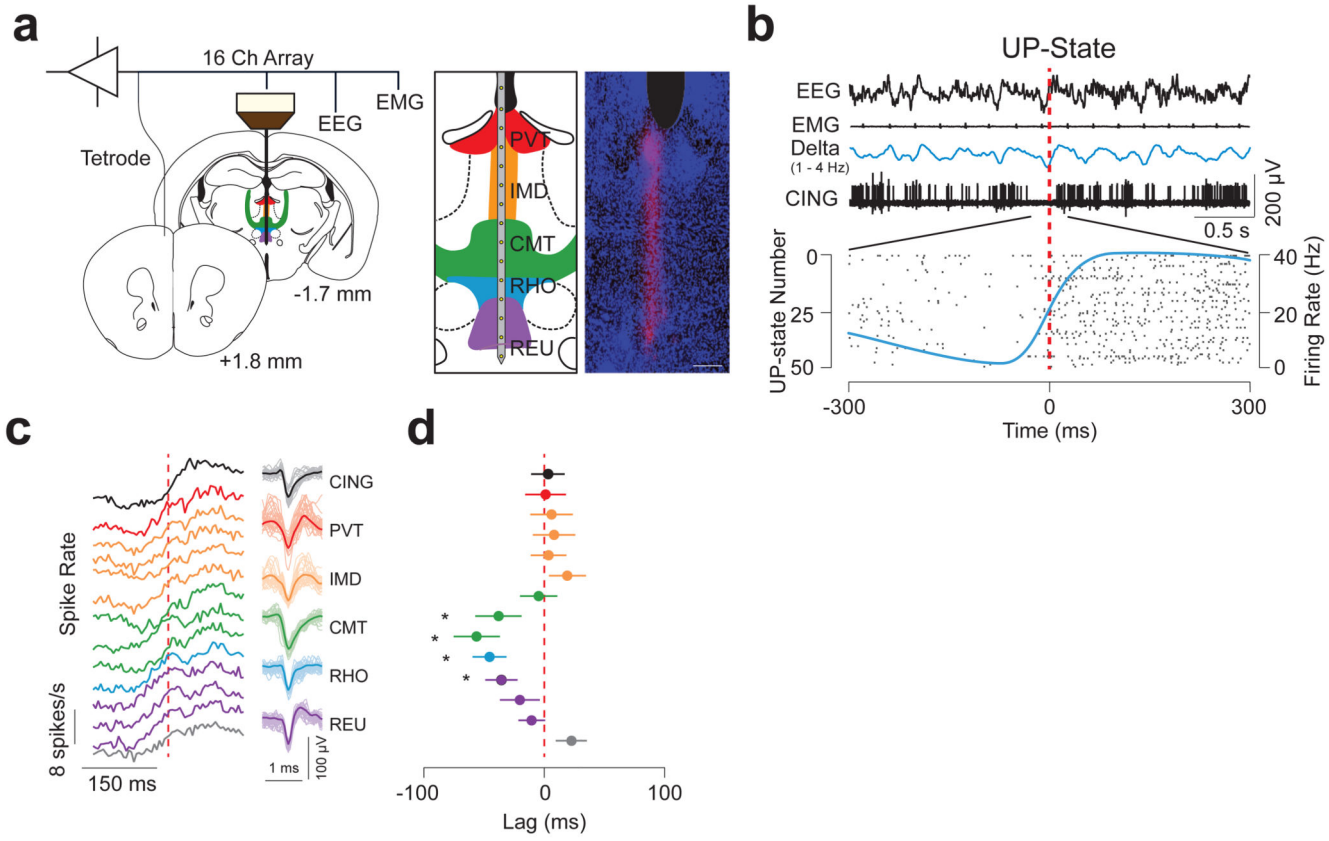

Figure 1. CMT neuron spiking is phase-advanced to cortical UP-states.

a, Schematic of instrumentation (left) for chronic recording from 16-channel linear array electrode in the midline thalamus and tetrode in CING in freely-moving mice. Illustration (middle) and anatomical verification (right) of the electrode array placement across the midline thalamic nuclei are shown. Scale bar: 150 µm. **b**, Representative EEG, EMG, LFPs and neuron unit recordings in CING during NREM sleep. Onset of the cortical UP-state is shown by the vertical dashed line (red) which corresponds to the detection of UP-states from the EEG based on zero-crossing (see Methods). Raster plot shows spiking activity from a representative CING neuron at the onset of 50 successively detected UP-states (bottom) recorded during spontaneous NREM. Average neuronal firing rate for the neuron (based on 10 ms bins) is shown by the blue solid line. Note the sigmoidal shape. **c**, Averaged spiking rate traces for each recording site (n = 13, 8, 8, 6, 6, 8, 7, 7, 8, 7, 7, 8, 8, 7 cells from top to bottom; during 28390 UP-states, from n = 6 animals) at the onset of the UP-state (dashed red line) during spontaneous NREM sleep. The grey plot indicates neurons recorded ventral to the midline thalamus. Representative spike waveforms for each nucleus are shown on the right. **d**, Averaged lags ± S.E.M. of half times from sigmoidal fits of spiking rates at the onset of cortical UP-state. Note the CMT neuron spike rate advancement over other thalamic and neocortical neurons. (CMT *vs* reuniens, rhomboideus, intermediodorsal, and paraventricular, P = 0.0073; f = 4.422; d.f. = 4; n = 22, 23, 7, 28 and 8 cells, respectively, n = 6 animals; one-way ANOVA;).

Europe PMC Funders Author Manuscripts

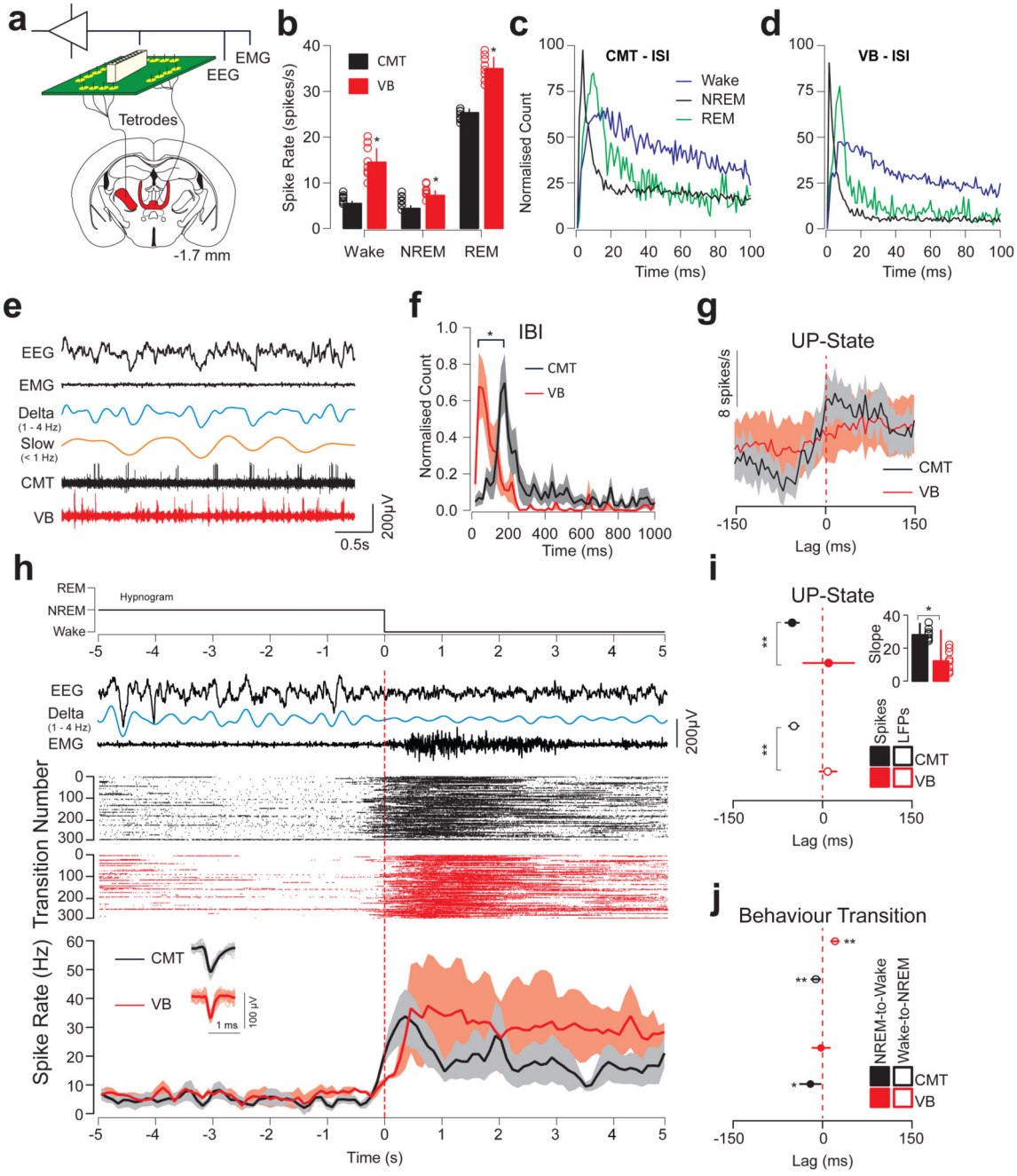

Figure 2. CMT neuron spiking is phase-advanced to sensory thalamus and to sleep-wake transitions.

a, Schematic of instrumentation for chronic simultaneous EEG/EMG and tetrode recording in CMT and VB in freely-moving mice. **b**, Averaged neuron spike rates ± S.E.M. of CMT (black) and VB (red) neurons across sleep-wake states (Wake: $P = 0.032$; $t = 3.71$; d.f. = 5; NREM: $P = 0.041$; $t = 3.00$; d.f. = 5; REM: $P = 0.0087$; $t = 4.55$; d.f. = 5; $n = 8$ cells per nucleus from 6 animals; one-sided t-test. **c**, **d**, Averaged inter-spike intervals of CMT (**c**) and VB (**d**) neurons during wake (black), NREM (blue) and REM (green) sleep states. Note the

sharp peak due to the bursting activity of thalamic neurons during NREM. **e**, Representative EEG/EMG traces and unit activity of CMT (black) and VB (red) neurons during NREM. Filtered delta (1 – 4 Hz) and slow oscillations (< 1 Hz) are shown. **f**, Inter-burst intervals (mean ± S.E.M.) of CMT (black) and VB (red) neurons during NREM. Peaks of inter-burst interval counts were significantly different for neurons in the two nuclei demonstrating the absence of phase-locking of neuron bursting in the two nuclei. ($P = 0.0064$; $t = 8.86$; d.f. = 10; two-sided *t*-test). **g**, Averaged spike rates ± S.E.M. of CMT (black) and VB (red) neurons at the onset of cortical UP-states (dashed red line) during spontaneous NREM. **h**, Representative Hypnogram, EEG/EMG, delta (filtered 1 – 4 Hz), CMT and VB neuronal spiking activity across NREM-to-Wake transitions. Raster plots show spiking activity for one representative cell in CMT (black) and VB (red) recorded concurrently from the same animal recorded over 300 successive NREM-to-Wake transitions during a 6-hour electrophysiological recording (ZT 3 – 9). Note that data was scored in 1-s epochs and microarousals were scored as wake events. Averaged neuronal firing rates ± S.E.M. for CMT ($n = 8$ cells; black) and VB ($n = 8$ cells; red; from $n = 6$ animals) neurons are shown across NREM-to-Wake transitions (bottom). Vertical lines (red dashed) indicate the onset of wakefulness. Representative spike waveforms are shown (bottom, inset). **i**, Averaged lags ± S.E.M. of CMT (black) and VB (red) neuron spike rate (solid) and LFP (open) at the onset of the cortical UP-states (red dashed line). Note the advancement of CMT neuron spiking to cortical UP-states compared to VB neuron spiking. ($P = 0.0008$; two-sided *t*-test; $t = 9.7$; d.f. = 6; one-sided *t*-test). Inset: slope of sigmoidal curve fits for CMT (black) and VB (red) neurons at the onset of the cortical UP-state. ($P = 0.017$, $t = 2.40$; d.f. = 14; two-sided *t*-test). **j**, Averaged lags ± S.E.M of CMT (black) and VB (red) neuron spiking rates across NREM-to-Wake and Wake-to-NREM transitions ($n = 8$ cells per nucleus from 6 animals). ($P = 0.027$; $t = 6.39$; d.f. = 6; two-sided *t*-test).

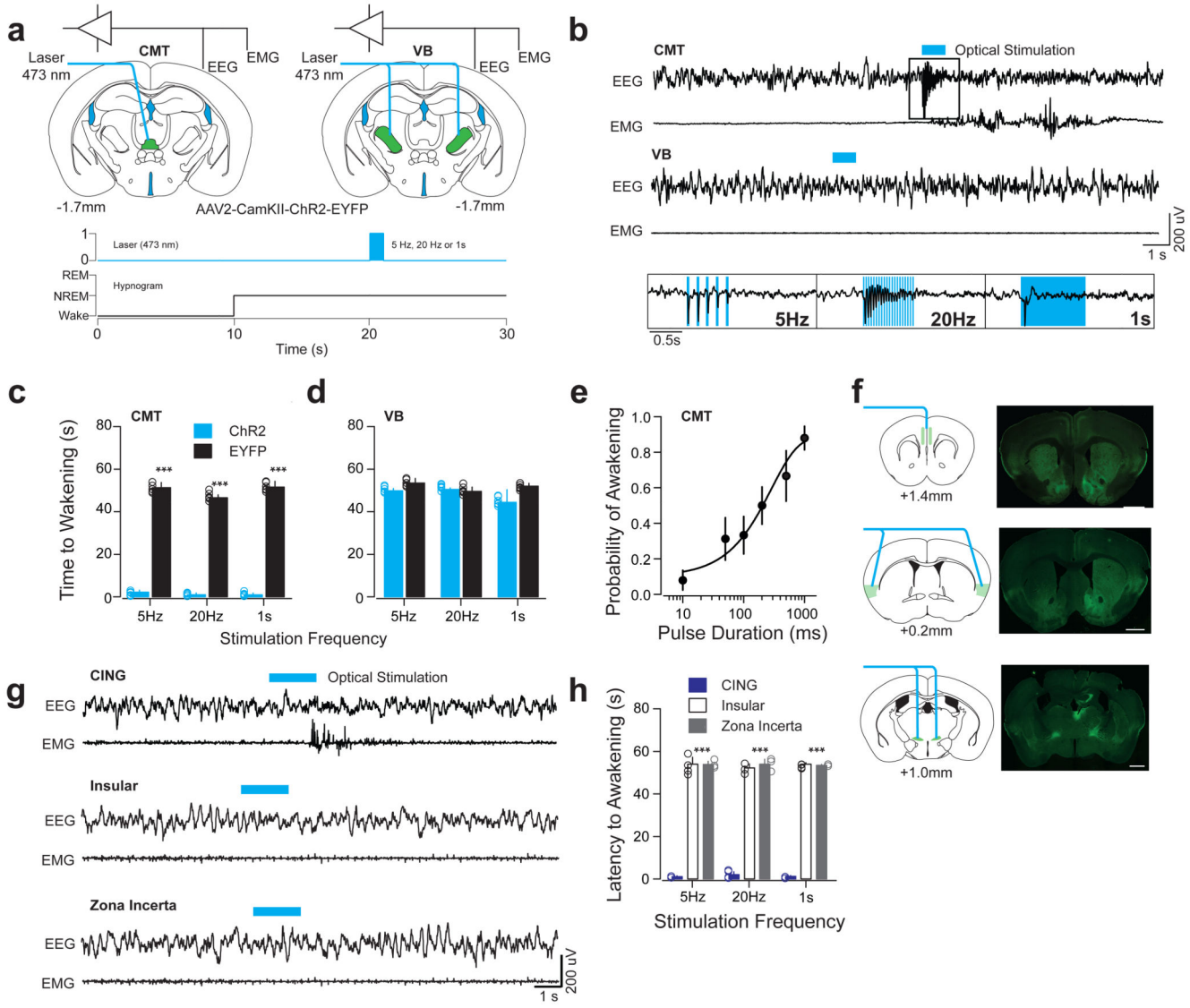

Figure 3. Optogenetic activation of CMT, but not VB, neurons entrains cortical UP-like states and induces arousal.

a, Schematic of a brain coronal section illustrating the *AAV2-CamKII-ChR2-EYFP* or *AAV2-CamKII-EYFP* (control) injection sites and chronic optical fiber implantation in CMT (left) and VB (right) areas. *Bottom*, experimental timeline showing blue optical stimulation trains (blue bar) delivered 10 s after the onset of NREM. **b**, Representative EEG/EMG traces from CMT (top) and VB (middle) illustrate arousal responses upon optogenetic activation. Note the high-fidelity entrainment of cortical activity upon optical activation of *ChR2-EYFP*-expressing CMT neurons at 5 and 20 Hz or continuous illumination (1 s, blue bar; bottom insets). **c**, **d**, Averaged latencies to awakening ± S.E.M. following optogenetic CMT (c) or VB (d) neuron activation ($n = 6$ animals per group). Data is based on a minimum of 10 stimulations per frequency per animal. (5 Hz: $P = 0.00008$; $t = 26.75$; d.f. = 10; 20 Hz: $P = 0.00006$; $t = 41.68$; d.f. = 10; 1 s: $P = 0.00006$; $t = 27.23$; d.f. = 10; two-sided t-test). **e**, Averaged probability of awakenings ± S.E.M. upon increasing

Europe PMC Funders Author Manuscripts

durations of single-pulse optogenetic CMT neuron activation. Values represent (Boltzmann sigmoidal curve fit, based on a minimum of 10 stimulations per duration per animal). **f**, Schematic for optogenetic activation of CMT axon terminals (left panels) and representative photomicrographs of coronal brain sections showing of *ChR2-EYFP*-expressing CMT axons (right panels) in CING (top), insular cortex (middle) and ZI (bottom). Scale bar: 1 mm. **g**, Representative EEG/EMG traces illustrate arousal response upon optogenetic activation of *ChR2-EYFP*-expressing CMT axons in CING (*top*), insular cortex (*middle*) and ZI (*bottom*) at various frequencies (5Hz, 20Hz, or continuous, 1 s; blue bar). Note the absence of awakenings upon activation of insular cortex or ZI. **h**, Averaged latencies to awakening ± S.E.M. upon optical activation of *ChR2-EYFP*-expressing CMT axon terminals in CING, insular cortex and ZI (minimum of 10 stimulations per frequency per animal, $n = 5$ animals per group). Note that stimulation of CING in non-transfected control animals did not induce awakening ($P = 0.00013$; $f = 2567$; d.f. = 2; two-way ANOVA).

Europe PMC Funders Author Manuscripts

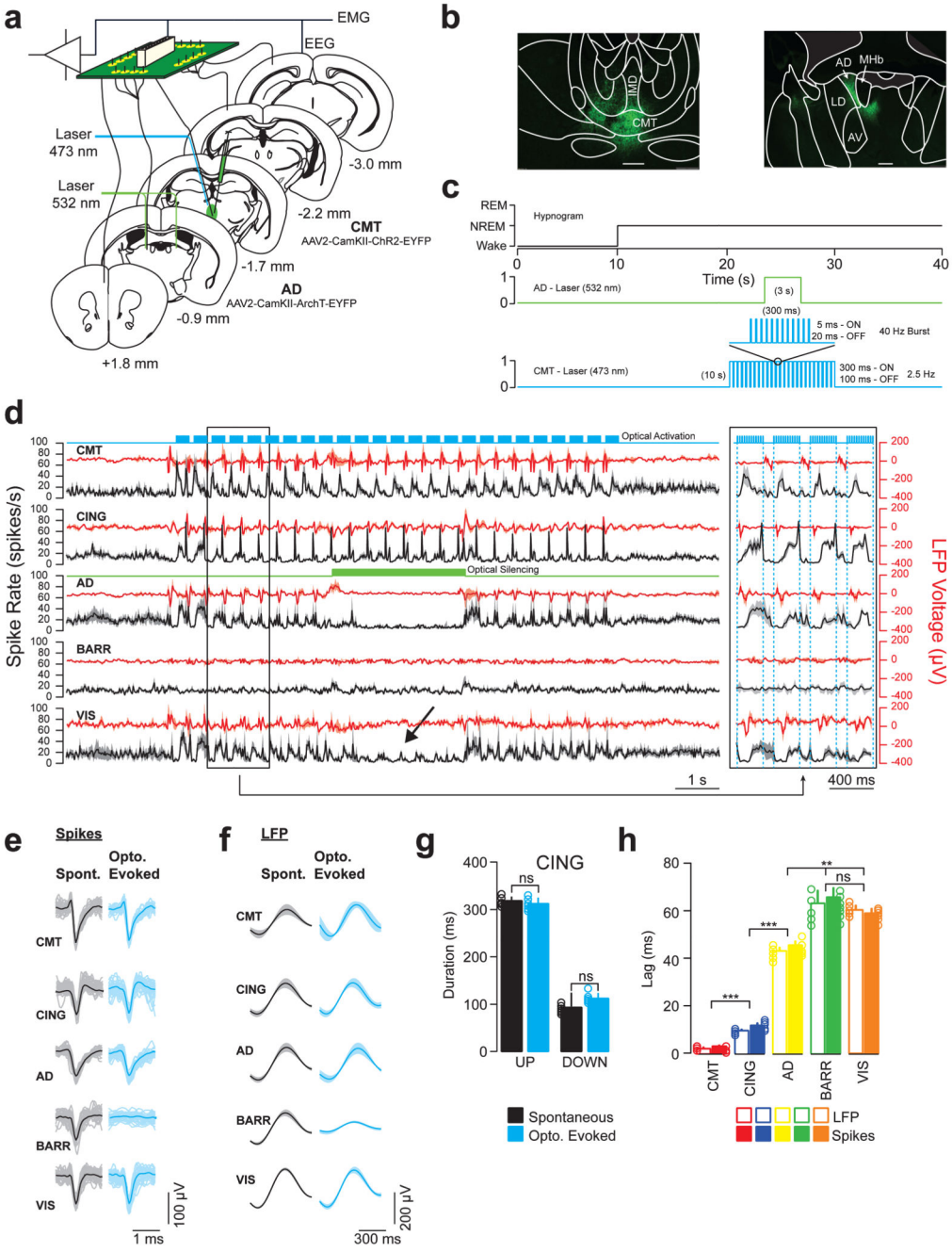

Figure 4. AD neurons relay CMT-induced UP-like states to posterior cortical areas.

a, Schematic of instrumentation for chronic implantation of multi-site tetrode recordings from CMT, CING, AD, BARR and VIS and optic fiber implants over CMT and AD (bilateral). *AAV2-CamKII-ChR2-EYFP* and *AAV2-CamKII-ArchT-EYFP* were stereotactically injected into CMT and AD (bilateral), respectively. **b**, Representative photomicrographs of coronal brain sections showing *ChR2-EYFP*-expressing CMT neurons (left) and *ArchT-EYFP* expressing AD neurons (right). Scale bar, 100 μm. Note the projections from CMT and AD neurons extending to the centro-lateral nucleus and internal

capsule, respectively. Data repeated in $n = 6$ animals. **c**, Experimental timeline showing blue optical activation of UP-like states (5 ms pulses, 300 ms ON, 100 ms OFF, 10 s duration) in CMT neurons and green optical silencing (3 s) of AD neurons, delivered 10 s after the onset of NREM. **d**, Averaged traces ± S.E.M. of CMT ($n = 9$ cells), CING ($n = 8$ cells), AD ($n = 9$ cells), BARR ($n = 9$ cells) and VIS ($n = 8$ cells; from $n = 6$ animals) neuron spiking activity (black) and LFP voltage (red) during combinatorial optogenetic experiments. Note the high-fidelity of CMT-induced UP-like states travelling along the CING-AD-VIS pathway and the complete blockade of spike transfer to VIS upon AD silencing (arrow). An expanded exert of the traces illustrating the lag of entrainment is shown on the right. **e**, Representative spike waveforms for spontaneous (black) and CMT-evoked (blue) neuronal firing in CMT, CING, AD, BARR and VIS. **f**, Average waveforms ± S.E.M. of spontaneous (black) and CMT-evoked (blue) UP-states in CMT, CING, AD, BARR and VIS. ($n = 8$ animals). **g**, Average durations of spontaneous (black) and evoked (blue) UP and Down states in CING (UP: $P = 0.45$; $t = 0.87$; d.f. = 7; DOWN: $P = 0.56$; $t = 0.66$; d.f. = 7; two-sided t-test; $n = 8$ animals; ns = not significant). **h**, Averaged neuron spiking and LFP lags ± S.E.M. from CMT (red), CING (blue), AD (yellow), BARR (green) and VIS (orange) upon optical activation of *ChR2-EYFP*-expressing CMT neurons. (CMT-to-CING: $P = 0.00009$; $t = 9.18$; d.f. = 8; CING -to-AD: $P = 0.000017$; $t = 22.35$; d.f. = 8; AD-to-BARR: $P = 0.0068$; $t = 3.621$; d.f. = 8; AD-to-VIS: $P = 0.0094$; $t = 7.18$; d.f. = 8; BARR-to-VIS: $P = 0.64$; $t = 0.49$; d.f. = 8; one-sided t-test; ns = not significant).

Europe PMC Funders Author Manuscripts

Europe PMC Funders Author Manuscripts

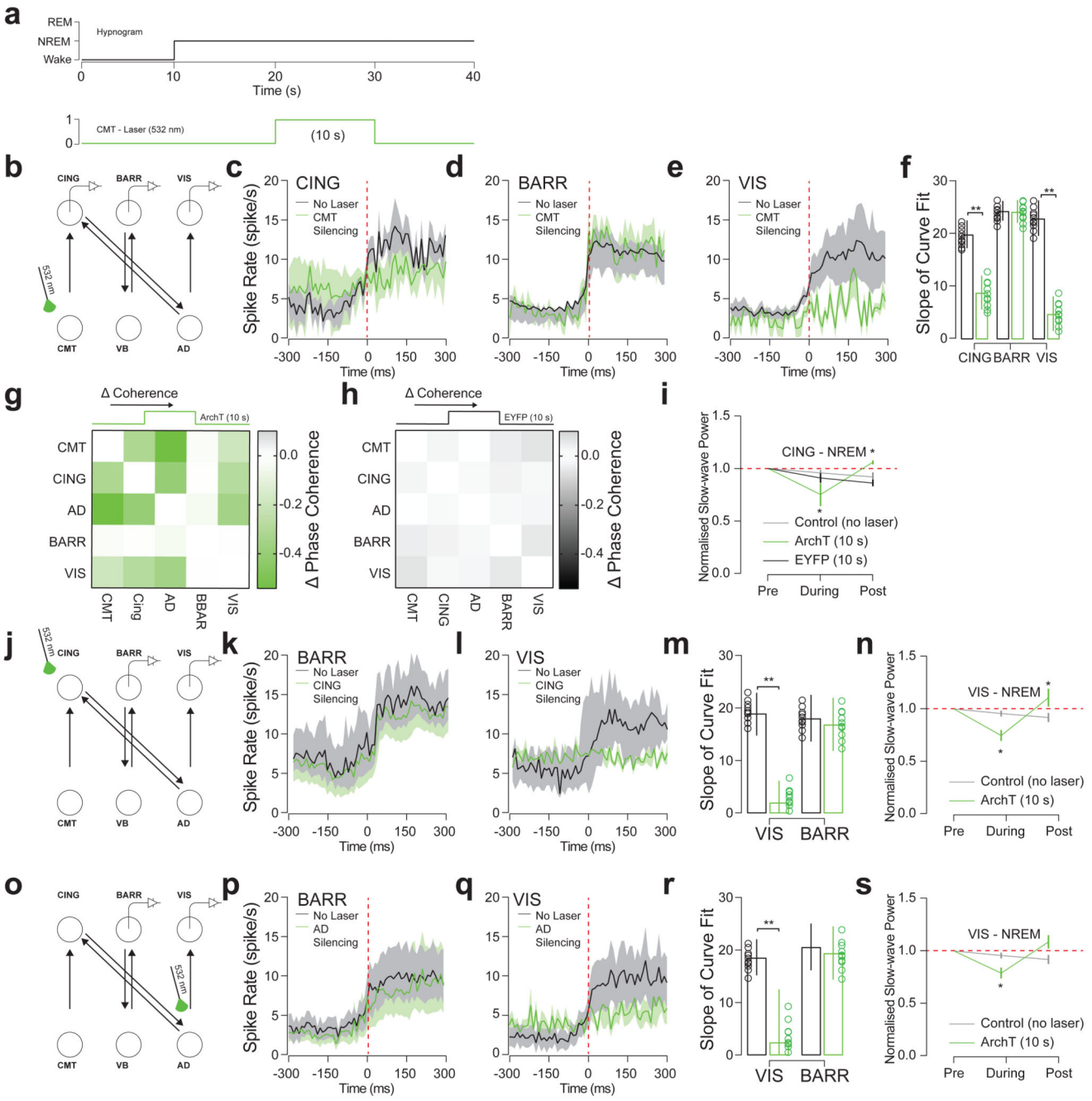

Figure 5. CMT neuron firing is necessary for cortical UP-state synchrony

a, Experimental timeline showing optical silencing (10 s, 532 nm) of ArchT-expressing CMT neurons 10 s after the onset of NREM. **b**, Schematic of N-type circuit and instrumentation for chronic implantation of multi-site tetrode recordings from CING, BARR and VIS and optic fiber implants over CMT. *AAV2-CamKII-ArchT-EYFP* was stereotactically injected into CMT. **c**, **d**, **e**, Average spiking rates ± S.E.M. for CING (**c**; n = 9 cells), BARR (**d**; n = 6 cells) and VIS (**e**; n = 8 cells; from n = 6 animals) neurons at the onset of the cortical UP-states (red dashed line). Note that silencing of *EYFP*-expressing

CMT neurons (control) did not significantly change spiking rates in CING ($P = 0.44$; $t = 1.74$; d.f. = 16; $n = 9$ cells; $n = 6$ animals; two-sided t-test). **f**, Average slope ± S.E.M. of curve fits for spiking rates at the start cortical UP-state. (CING: $P = 0.008$; $t = 2.66$; d.f. = 16; $n = 9$ cells; BARR: P = 0.96; $t = 0.05$, d.f. = 10; $n = 6$ cells; VIS: $P = 0.002$; $t = 3.87$; d.f. = 14; $n = 8$ cells; from $n = 6$ animals; two-sided t-test). **g, h**, Averaged change in phase coherence for CMT, CING, AD, BARR and VIS for optical silencing of CMT neurons expressing *ArchT-EYFP* (**g**) and *EYFP* (**h**). **i**, Averaged delta power ± S.E.M. of LFP signals recorded in CING 10 s before, during and 10 s after optogenetic silencing of ArchT-(green) or EYFP-(black) expressing CMT neurons compared to control conditions (grey). Delta power is normalized to the first 10 s of NREM. Note the rebound in delta activity after CMT neuron silencing (dotted red line). ($P = 0.005$; two-sided t-test; $t = 5.02$; d.f. = 5; $n = 6$; animals compared to normalized value 1). **j**, Schematic of N-type circuit and instrumentation for chronic implantation of multi-site tetrode recordings from BARR and VIS and optic fiber implants over CING. *AAV2-CamKII-ArchT-EYFP* was stereotactically injected into CING. **k**, **l**, Average spiking rates ± S.E.M. for BARR (**k**; $n = 6$ cells) and VIS (**l**; $n = 6$ cells; from $n = 5$ animals) neurons at the onset of the cortical UP-states (red dashed line). **m**, Average slope ± S.E.M. of curve fits for spiking rates at the start cortical UP-state. (BARR: $P = 0.86$; $t = 1.02$; VIS: $P = 0.014$; $t = 3.99$; d.f. = 4; two-sided t-test;). **n**, Averaged delta power ± S.E.M. in VIS 10 s before, during and 10 s after optogenetic silencing of ArchT-expressing CING neurons (green; $P = 0.036$; one-sided t-test; $t = 3.99$; d.f. = 3; one-sided t-test; from $n = 5$ animals) and control conditions (grey). Delta power is normalized to the first 10 s of NREM. Note the rebound in delta activity after CMT neuron silencing (dotted red line; $P = 0.039$; one-sided t-test; $t = 3.45$; d.f. = 3; one-sided t-test; compared to normalized value 1). **o**, Schematic of N-type circuit and instrumentation for chronic implantation of multi-site tetrode recordings from BARR and VIS and optic fiber implants over AD. *AAV2-CamKII-ArchT-EYFP* was stereotactically injected into AD. **p**, **q**, Average spiking rates ± S.E.M. for BARR (**p**; $n = 9$ cells) and VIS (**q**; $n = 10$ cells; from $n = 6$ animals) neurons at the onset of the cortical UP-states (red dashed line). **r**, Average slope ± S.E.M. of curve fits for spiking rates at the start cortical UP-state. BARR: $P = 0.75$; $t = 1.73$; d.f. = 7; $n = 9$ cells; VIS: $P = 0.036$; $t = 6.84$, d.f. = 8; $n = 10$ cells; $n = 6$ animals; two-sided t-test). **s**, Averaged delta power ± S.E.M. in VIS 10 s before, during and 10 s after optogenetic silencing of ArchT-expressing AD neurons (green) and control conditions (grey). Delta power is normalized to the first 10 s of NREM. Note the rebound in delta activity after CMT neuron silencing (dotted red line; $P = 0.011$; $t = 4.63$; d.f. = 4; from $n = 6$ animals; one-sided t-test; compared to normalized value 1).

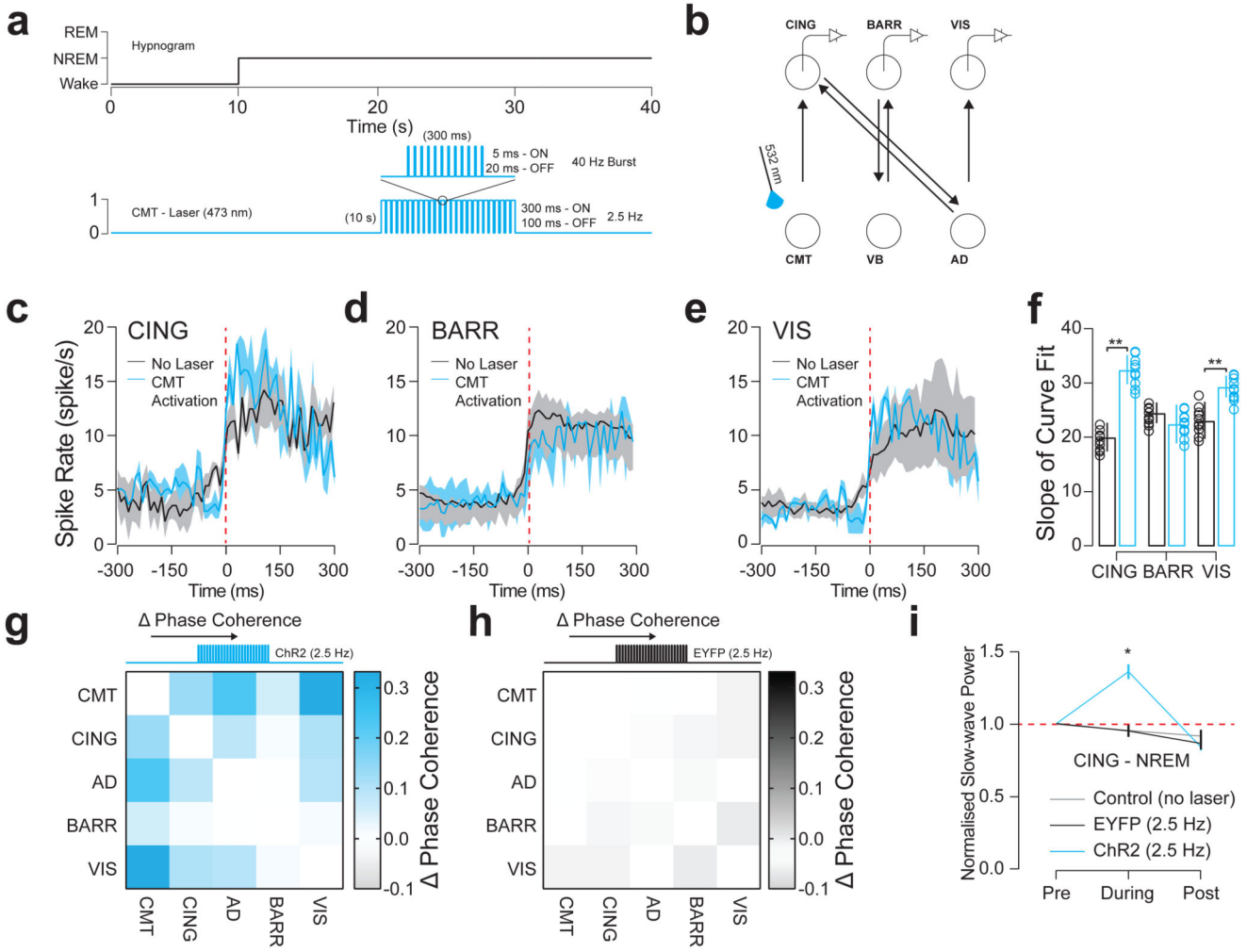

Figure 6. CMT neuron firing increases synchrony of cortical UP-states

a, Experimental timeline showing optogenetic activation of UP-like states (5 ms, 300 ms ON, 100 ms OFF, 10 s duration) in CMT neurons delivered 10 s after the onset of NREM. **b**, Schematic of N-type circuit and instrumentation for chronic implantation of multi-site tetrode recordings from CING, BARR and VIS and optic fiber implants over CMT. *AAV2-CamKII-ChR2-EYFP* was stereotactically injected into CMT. **c**, **d**, **e**, Average spiking rates ± S.E.M. for CING (**c**; $n = 8$ cells), BARR (**d**; $n = 6$ cells) and VIS (**e**; $n = 7$ cells; from $n = 6$ animals) neurons at the onset of the cortical UP-states (red dashed line; spontaneous: black; evoked: blue). **f**, Average slope ± S.E.M. of curve fits for spiking rates at the start cortical UP-state. (CING: $P = 0.004$; $t = 3.29$; d.f. = 16; $n = 8$ cells; BARR: $P = 0.62$; $t = 0.51$, d.f. = 12; $n = 6$ cells; VIS: $P = 0.013$; $t = 2.58$; d.f. = 14; $n = 7$ cells; from $n = 6$ animals; two-sided *t*-test) **g**, **h**, Averaged change in phase coherence for CMT, CING, AD, BARR and VIS for blue optical activation of CMT neurons expressing *ChR2-EYFP* (**g**) and *EYFP* (**h**). **i**, Averaged delta power ± S.E.M. in CING 10 s before, during and 10 s after optogenetic activation of CMT neurons expressing *ChR2-EYFP* (blue), EYFP (black) and control

Europe PMC Funders Author Manuscripts

conditions (grey). Delta power is normalized to the first 10 s of NREM. ($P = 0.0006$; $t = 7.59$; d.f. = 5; $n = 6$ animals; two-sided t-test).

Europe PMC Funders Author Manuscripts

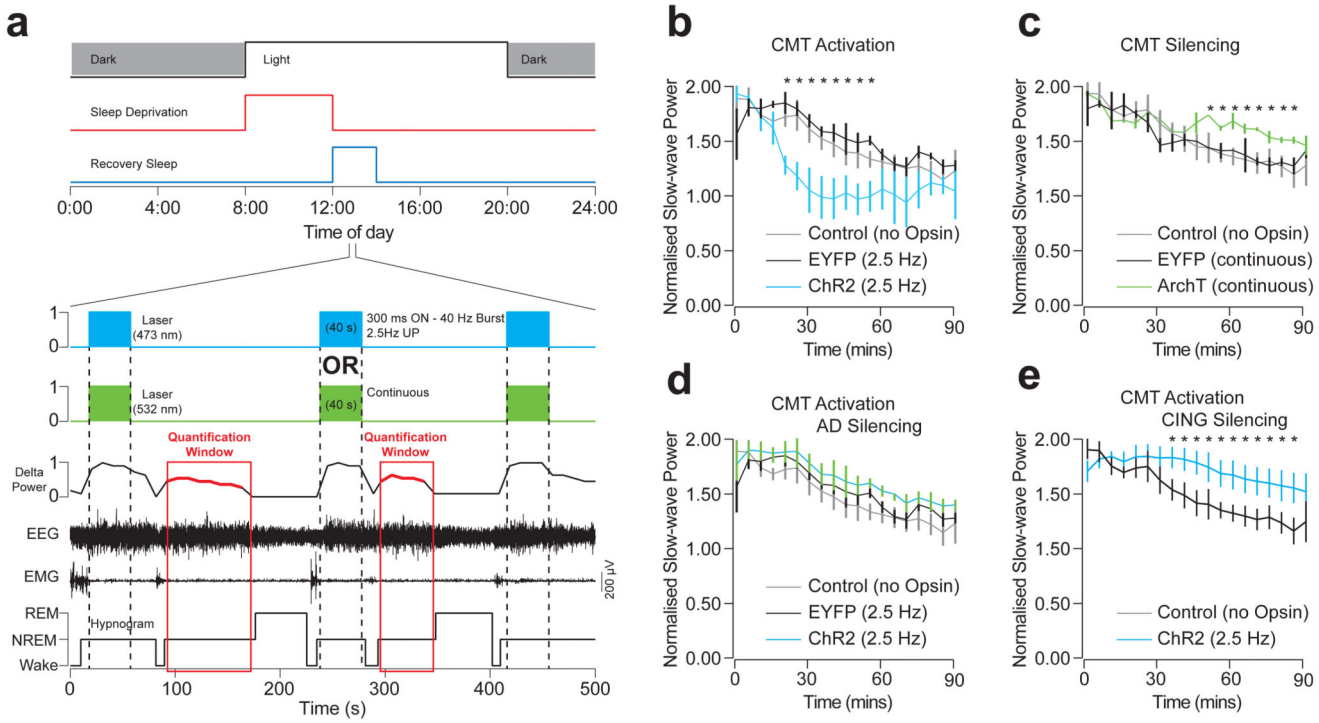

Figure 7. CMT neuron activity promotes sleep recovery.

a, Experimental timeline showing sleep deprivation and sleep recovery protocols. *ChR2-EYFP* expressing CMT neurons were activated with blue light (300m ON, 100ms OFF, 40 s duration) and *ArchT-EYFP* expressing CMT silenced with green light (40 s continuous) during every second NREM period during recovery sleep. The rebound delta power was measured from the interleaving NREM periods. **b**-**e**, Average delta power ± S.E.M. during sleep recovery in CING during optogenetic stimulation of UP-states in CMT neurons (**b**: $P < 0.035$; $t = 4.59$; d.f. = 7; one-way ANOVA; $n = 6$ animals), optogenetic silencing of CMT neurons (**c**: $P < 0.027$; $t = 3.86$; d.f. = 5; one-way ANOVA; $n = 6$ animals), optogenetic stimulation of CMT neurons with concurrent optogenetic silencing of AD neurons (**d**: $P = 0.25$; $t = 1.74$; d.f. = 5; one-way ANOVA; $n = 6$ animals) and optogenetic silencing of CING neurons (**e**: $P = 0.013$; $t = 5.68$; d.f. = 4; one-way ANOVA; $n = 5$ animals).